

MACHINE LEARNING ASSISTED APPROACH TO DESIGN LATTICES  
WITH PRESCRIBED BANDGAP CHARACTERISTICS

by  
Mohamed Shendy

A Thesis presented to the Faculty of the  
American University of Sharjah  
College of Engineering  
In Partial Fulfilment  
of the Requirements  
for the Degree of  
  
Master of Science in  
Mechanical Engineering

Sharjah, United Arab Emirates

March 2023

## Declaration of Authorship

I declare that this thesis is my own work and, to the best of my knowledge and belief, it does not contain material published or written by a third party, except where permission has been obtained and/or appropriately cited through full and accurate referencing.

Signed..........

Date.....13/03/2023.....

The Author controls copyright for this report.

Material should not be reused without the consent of the author. Due acknowledgement should be made where appropriate.

© Year 2023

Mohamed Shendy

ALL RIGHTS RESERVED

## Approvals

We, the undersigned, approve the Masters Thesis written by:

Thesis Title:

Date of Defense:

**Name, Title and Affiliation**

**Signature**

---

Dr.  
Professor/Associate Professor/Assistant Professor  
Department of  
Thesis Advisor

---

Dr.  
Professor/Associate Professor/Assistant Professor  
Department of  
Thesis Co-advisor

---

Dr.  
Professor/Associate Professor/Assistant Professor  
Department of  
Thesis Examiner (Internal)

---

Dr.  
Professor/Associate Professor/Assistant Professor  
Department of  
University Name:  
Thesis Examiner (External)

Accepted by:

Dr.  
Dean  
College/School of

Dr. Mohamed El-Tarhuni  
Vice Provost for Research and Graduate Studies  
Office of Research and Graduate Studies

## **Acknowledgments**

I would like to thank my advisors, Dr. Maen Alkhader and Dr. Bassam Abu-Nabah, for providing knowledge, guidance, support, and motivation throughout my research stages. I'm deeply indebted for their great assistance, worthy discussions, and invaluable suggestions. I would also like to express my appreciation to Dr. Mohammad Jaradat for providing knowledge, advising and guidance on the machine learning part of this thesis. I would also like to thank the professors of the Mechanical Engineering department who taught me during my graduate study journey at the American University of Sharjah. Their teaching methods and knowledge inspired and motivated me. I want to thank the American University of Sharjah for financially supporting me during my studies through a graduate teaching assistantship.

## **Dedication**

To my family...

## Abstract

Lattice-based metamaterials belong to the phononic crystals class of materials which are known for their ability to interact with, direct, and block elastic waves. These properties made lattice-based metamaterials appealing in wave guiding, noise filtering, and vibration isolation applications. However, capitalizing on the full potential of lattice-based materials in isolation and filtering applications has been hindered by the lack of systematic and efficient design methodologies capable of producing a lattice with pre-set band gap characteristics. Existing design methodologies utilize time-consuming iterative computational schemes and often move towards geometrically complex lattices whose fabrication requires expensive additive manufacturing techniques. This work proposes an artificial intelligent-assisted design methodology that integrates sinusoidal perturbations and the easy-to-fabricate double-wall hexagonal lattice. In the proposed approach, sinusoidal perturbations with different frequencies and amplitudes are superposed on the double-wall hexagonal lattice to increase the number and bandwidth of its band gaps. Finite element analysis is used to determine the band gaps in the perturbed lattices. By using five perturbation frequencies, five amplitudes, and six lattice porosities, the perturbed lattices delivered a band gap at each frequency in the range of 0 to 1000kHz. Machine learning, namely deep neural networks, is used to model the relationships among the perturbation parameters, lattice porosity, and the corresponding band gap characteristics. Three parallel neural network models are developed. These predict the maximum number of band gaps and the width and centroid of the band gap with maximum bandwidth. Results showed that the developed neural network models had an average accuracy of 90%. The developed neural network models constitute the core of the proposed design methodology. They are used to determine the coarse design parameters (i.e., porosity and perturbation parameters) required to realize prescribed band gap characteristics. The coarse design parameters are subsequently refined using finite element analysis. This approach accelerates the design process and eliminates the need for time-expensive iterative processes. A case study is presented to demonstrate the efficiency and practicality of the proposed design process.

**Keywords:** Lattice materials, Metamaterials, Band gaps, Finite element, Honeycomb lattice, Acoustic characteristics, Neural Networks

## Table of Contents

Abstract	6
List of Figures	8
List of Tables	10
Chapter 1. Introduction	11
1.1. Introduction	11
1.2. Overview	11
1.3. Thesis Objectives	11
1.4. Research Contribution	12
1.5. Thesis Organization	12
Chapter 2. Background and Literature Review	13
Chapter 3. Methodology	17
3.1. Design Methodology	17
3.2. Parent Lattice Structure and Material	18
3.3. Superposing Periodic Sinusoidal Perturbation	19
3.4. Band Gap Determination Using Finite Element Analysis	21
3.5. Prediction of Band Gaps Using Machine Learning (ML)	24
Chapter 4. Results	28
4.1. Verification of The Finite Element-Approach and Its Implementation	28
4.2. Bandgaps of The Unperturbed Double-Sided Honeycomb	28
4.3. Band Gaps of The Perturbed Double-Sided Honeycomb	29
4.4. MANNs Implementations for The Three Key Aspects:	35
Chapter 5. Discussion	40
Chapter 6. Conclusion	44
Vita	51

## List of Figures

Figure 1 Schematic representation of the artificial intelligence-assisted approach for designing lattice materials with prescribed band gaps.	17
Figure 2 Parent lattice structure, showing its geometry and main features.	18
Figure 3 Schematics of the sinusoidal perturbations superposed on cell walls	19
Figure 4 Examples demonstrating the geometry of the double-sided honeycomb lattice after the sinusoidal perturbation is applied ( $A_n=0.3$ )	21
Figure 5 Schematics of the unit cells used in the finite element analysis to represent both unperturbed and perturbed honeycomb lattices.	21
Figure 6 The 1st Brillion zone corresponding to the unit cell of Figure 5	22
Figure 7 The band gap structure of the unperturbed honeycomb lattice with 15% relative density	24
Figure 8 Schematic diagram of the implemented parallel multilayer ANNs	25
Figure 9 Feed forward multilayer MANN architecture	26
Figure 10 Block diagram of the training process for MANN using supervised learning	27
Figure 11 Eigenfrequencies of single-sided aluminum honeycomb hexagonal lattice with the relative densities of 5%,10%,15%, and 30%. The analyzed lattice . and shown results are identical to those presented in reference [11].	28
Figure 12 Eigenfrequencies of double-sided aluminum honeycomb hexagonal lattice with the relative densities of 5%, 10%, 15%, 20%, 25%, and 30%.	29
Figure 13 Band gaps of perturbed double-sided aluminum honeycomb hexagonal lattice, showing the band gaps for the perturbation amplitudes of 0.1,0.2,0.3,0.4 and 0.5; perturbation frequencies of 0.5, 2, 4, 6 and 10 (cycles); and relative densities of 5%, 10%, 15%, 20%, 25%, and 30%.	31
Figure 14 Key band gap features at 5% relative density, showing (A) the size of widest band gap (S.O.W.B) in kHz, (B) its centroid (C.O.W.B) in kHz and (C) the number of band gaps.	32
Figure 15 Key band gap features at 10% relative density, showing (A) the size of widest band gap (S.O.W.B) in kHz, (B) its centroid (C.O.W.B) in kHz and (C) the number of band gaps.	32

- Figure 16 Key band gap features at 15% relative density, showing (A) the size of widest band gap (S.O.W.B) in kHz, (B) its centroid (C.O.W.B) in kHz and (C) the number of band gaps. 33
- Figure 17 Key band gap features at 20% relative density, showing (A) the size of widest band gap (S.O.W.B) in kHz, (B) its centroid (C.O.W.B) in kHz and (C) the number of band gaps. 34
- Figure 18 Key band gap features at 25% relative density, showing (A) the size of widest band gap (S.O.W.B) in kHz, (B) its centroid (C.O.W.B) in kHz and (C) the number of band gaps. 34
- Figure 19 Key band gap features at 30% relative density, showing (A) the size of widest band gap (S.O.W.B) in kHz, (B) its centroid (C.O.W.B) in kHz and (C) the number of band gaps. 34
- Figure 20 Performance of the MANN proposed for predicting the maximum band gap width exhibited by the sinusoidally perturbed hexagonal honeycomb. A) shows MSE plot and B) shows the regression plots. 37
- Figure 21 Performance of the MANN proposed for predicting the number of band gaps exhibited by the sinusoidally perturbed hexagonal honeycomb. A) shows MSE plot and B) shows the regression plots. 38
- Figure 22 Performance of the MANN proposed for predicting the centroid of the band gap with maximum width. A) shows the MSE plot and B) shows the regression plots. 38
- Figure 23 Design Point#2 perturbed unit cell and its corresponding band structure to demonstrate the accurate overlapping between its exhibited widest band gap and the prescribed band gap frequency range. 43

## List of Tables

- Table 1 The mean error (%) of the MANN proposed for predicting the maximum band gap width exhibited by the sinusoidally perturbed hexagonal honeycomb. Table shows the effect of relative density ( $\rho^*$ ) and perturbation frequency (n). The mean error (%) is compute by averaging the errors corresponding to a range of perturbation amplitudes ( $A_n$ ). 37
- Table 2 The mean error (%) of the MANN proposed for predicting the number of bandgaps exhibited by the sinusoidally perturbed hexagonal honeycomb. Table shows the effect of relative density ( $\rho^*$ ) and perturbation frequency (n). The mean error (%) is compute by averaging the errors corresponding to a range of perturbation amplitudes ( $A_n$ ). 38
- Table 3 The mean error (%) of the MANN proposed for predicting the centroid of the band gap with maximum width in the sinusoidally perturbed hexagonal honeycomb. Results show the effect of relative densities and perturbation frequency (n). The mean error (%) is compute by averaging the errors corresponding to a range of perturbation amplitudes ( $A_n$ ). 39
- Table 4 MANNs' predicted perturbation parameters corresponding to the frequency band gap between 575 kHz and 625kHz. 43

## **Chapter 1. Introduction**

### **1.1. Introduction**

This chapter briefly introduces lattice metamaterials and their ability to deliver unique acoustic properties that fit a wide range of noise filtering and isolation applications. In addition, this chapter presents the problem investigated in this thesis and highlights this work's contributions. Finally, the general organization of the thesis is presented.

### **1.2. Overview**

Recently, Lattice-based Metamaterials have acquired significant interest due to their ability to exhibit directional acoustic properties and frequency band gaps. These properties made lattice-based metamaterials ideal candidates for vibrational filtering and isolation applications. Although lattice-based metamaterials can exhibit a wide range of frequency band gaps, designing metamaterials with pre-set band gap characteristics has been challenging and expensive. Currently used approaches in designing lattice-based metamaterials either utilize forward iterative methods, which can be prohibitively time-consuming if used to design lattice materials with pre-set band gaps or result in lattice topologies whose manufacturing requires expensive 3D printing technologies. Accordingly, though useful, lattice-based materials have yet to be used to their full capacity. This work draws on recent efforts which showed that the band gaps of lattice materials could be increased in number and width by superposing parametric-based curvatures on their cell walls [1]–[4]. By imposing sinusoidal perturbations on the cell walls of double-sided regular honeycombs with different porosities, this work aims to create an easy-to-fabricate lattice with a rich band gap structure that can deliver a frequency band gap at any frequency below the 1000kHz limit. Subsequently, this work utilizes machine learning to accelerate the design process and relate the sinusoidal perturbation parameters to their corresponding band gap characteristics. Users can use the developed machine learning models to create lattice materials with pre-set band gap characteristics while eliminating the currently used time-consuming iterative processes.

### **1.3. Thesis Objectives**

The overarching goal of this thesis is to create a systematic method for designing lattice metamaterials with prescribed band gap characteristics. This goal is satisfied by

achieving multiple objectives. First, this work aims to demonstrate the possibility of creating band gaps at any frequency from 0 to 1000kHz through superposing sinusoidal perturbations on the simple hexagonal double-sided lattice. Second, this work aims to create lattices whose manufacturing does not require expensive 3D printing technologies. To this end, this work adopts the double-sided honeycomb lattice which is often fabricated using conventional machining (e.g., corrugation and welding). Third, this work aims to develop machine learning models that can accurately model the relationship between the parameters of the imposed sinusoidal perturbations and their corresponding band gaps. Finally, this work aims to show, though a case study, the practicality and accuracy of the developed machine learning models in designing lattice metamaterials with pre-set band gap characteristics.

#### **1.4. Research Contribution**

The contributions of this research work can be summarized as follows:

- Enhance the number and width of the band gaps exhibited by the double-sided hexagonal honeycomb lattice through superposing sinusoidal perturbations.
- Perform a parametric study to show the effect of perturbation parameters (i.e., amplitude and frequency) and relative density on the band gap properties of the double-sided hexagonal lattice.
- Propose a machine learning-based model to predict the band gap characteristics corresponding to any combination of relative density, perturbation frequency, and perturbation parameters.
- Using a case study, show the feasibility of the proposed artificial intelligence-assisted design approach to create metamaterials with pre-set band gap characteristics.

#### **1.5. Thesis Organization**

The rest of the thesis is organized as follows: Chapter 2 presents the Background and Literature review. Chapter 3 discusses the Methodology. Chapter 4 presents the Results and Discussion. Finally, the conclusions are listed in Chapter 5.

## Chapter 2. Background and Literature Review

Periodic lattice structures have been known for their ability to deliver high stiffness, strength, and energy absorption capacity to weight ratios [5]–[8]. These unique structural properties made them appealing to industries that favor lightweight materials, such as the aerospace and wind energy (turbines) industry [9], [10]. Lately, periodic lattice structures have acquired significant interest for their ability to deliver tunable acoustic properties that can be used in wave guiding, filtering, and sensing applications. Tunable acoustic properties include natural frequencies, natural modes, band gaps and phase velocities. One can control waves propagating through a lattice material by tuning these properties. Tuning the properties mentioned above can be accomplished by exploiting the internal topology of periodic lattice structures. Multiple examples in the literature showed that altering the topology of a lattice can change its acoustic properties [11]–[18]. These efforts showed that topological parameters such as relative density, ligament length, ligament slenderness ratio and topological imperfections (e.g., imperfections induced by damage caused by excessive loading) strongly affect the acoustic properties of lattice materials. Relative density (i.e., 1-porosity) represents the solid phase volume fraction of a lattice material [19], [20].

Multiple efforts have investigated the sensitivity of waves propagating in lattice materials to relative densities, length of ligaments, and slenderness ratio [11], [17], [21]. In reference [17], the fundamentals of band gap formation in lattice materials were investigated by analyzing wave behavior in well-known lattice structures (Square, Triangular, Kagome, and hexagonal honeycomb lattices). This study concluded that the triangular and hexagonal honeycomb lattices exhibit wider band gaps than the other lattice structures, particularly at higher relative densities. In reference [11], a parametric study was conducted to assess the effect of relative density (i.e., between 5% and 20%) on wave propagation characteristics of honeycombs. The parametric study showed that relative density increase is associated with a decrease in the band gap frequencies appearing below the 100kHz threshold. Also, this study assessed the feasibility of utilizing non-destructive ultrasonic testing methods to detect damage in aluminum honeycombs subjected to stretching loadings. The feasibility was assessed by analyzing the sensitivity of the lattice's band gaps to deformations induced by stretching loads. In reference [21], waves propagating in 3D-based lattice materials (e.g., Kelvin, simple

cubic, octet, framed-cubic lattices) were investigated. These 3D- based lattice materials are the three-dimensional extension of the two-dimensional lattices examined in [17]. The study showed that 3D lattice materials exhibit different wave propagation behavior than their corresponding 2D lattice materials.

The efforts mentioned above, which investigated multiple topologies, showed that investigated lattice metamaterials often exhibit limited and narrow band gaps. Lattices with this observed behavior are impractical and incompatible with vibrational isolation applications. Vibrational isolation applications require lattices that block or interact with waves at specific frequency ranges. The investigated lattices are not readily functional at the frequencies needed by industrial applications. Therefore, multiple efforts have imposed systematic geometrical features to reshape the walls of lattice-based metamaterials to optimize their band gap properties for vibrational isolation applications. Imposing geometrical features such as Koch fractal on the straight cell walls square and triangular lattice metamaterials to optimize their band gap properties have been proposed in References [1], [2]. These studies showed that the imposing Koch fractal with different fractality levels on the cell walls of lattice metamaterial leads to wider band gaps than as compared to the band gaps exhibited by the parent lattice structure. Increasing the fractality ratio shifted the band gaps to a lower frequency range. Parametric-based curvatures were imposed on the cell walls of lattice-based metamaterials to optimize their band gap properties [3], [4]. Superposing spline-like shapes [3] and sinusoidal-like shapes on cell walls of lattice-based metamaterial were explored. These efforts used parametric studies [4] and optimization algorithms (e.g., adjoint sensitivity method) [3]. Both perturbation techniques resulted in wider band gaps. These perturbations were also considered in enhancing the buckling strength of honeycombs [22]. A different class of geometrical modification was explored to enhance lattice materials' band gaps. The geometry of a square lattice material was modified by including a core embedment [23]. Different geometrical core configurations were considered (i.e., square core, circular core, and re-entrant core). Embedded enhanced wave transmission isolation, and therefore, the proposed technique was proposed for vibrational isolation applications.

Modifying lattice geometry by applying loads was explored [24], [25]. These efforts showed that applying external loads on lattices can cause significant elastic

deformations, which affect their multiband gap properties. Considered deformations were induced by bi-axial compression and magnetic actuation. Both loading techniques were found to be able to change the band gap size and band gap location in the examined frequency ranges. Therefore, these techniques were proposed to develop metamaterials compatible with filtering and multi-switches applications.

Band gap characteristics of lattice materials are usually obtained using mathematical and finite element methods. Fast models based on the plane wave expansion methods (PWE) were proposed to predict the band structure of lattice metamaterials [26], [27]. However, the accuracy of these models decreased as the size of the lattice decreased. On the other hand, multi-scale finite element methods showed better accuracy in predicting the band structure of heterogenous lattice metamaterials, even with subjectively coarse meshes [27].

The emergence of Artificial Intelligence (AI) and its developed capabilities has led the material science and industry community to acknowledge its importance. Machine learning techniques such as deep learning and hybrid intelligent systems (NN-GA) have been utilized in predicting optimal truss architectures that can be utilized effectively in a desirable application [28], [29]. Structural optimization was done to attain unique mechanical properties to be ideally suited for applications ranging from lightweight structures to biomimetic implants. The complexity in attaining a direct relation for the failure of an alloyed metal experiencing tensile deformation was solved through ML techniques. Artificial neural networks have been used to predict the evolution of local strain distribution, plastic anisotropy, and failure caused by the tensile loading of ALSi10Mg Aluminum alloy [30].

This work proposes an artificial intelligence-assisted design approach to develop lattice metamaterial with prescribed band gaps. In this approach, sinusoidal perturbations are imposed on the cell walls of double-sided hexagonal honeycombs with different relative densities. Subsequently, a parametric study is conducted to investigate the effect of imposed sinusoidal perturbations on the band gap properties. The parameters considered in the parametric study are relative density, perturbation frequency, and perturbation amplitude. The parametric study is focused on the behavior of the widest band gap, its centroid and the number of band gaps. Machine learning is then used to model the relationship between perturbation parameters and relative density on one side

and band gap characteristics on the other. The proposed machine learning models can assist in designing lattice metamaterials with pre-set band gap characteristics.

## Chapter 3. Methodology

### 3.1. Design Methodology

The artificial intelligence-assisted design process, schematically shown in Figure 1, used in this work to develop lattice metamaterials with prescribed band gaps involves five sequential steps: First, a periodic lattice material is selected. This lattice material is considered a parent lattice. It may exhibit very few, very narrow, or undesirable band gaps. Second, the band gaps of the parent lattice are enhanced by increasing their number and width through superposing periodic perturbations with various frequencies and amplitudes on the parent lattice. The band gaps of the periodic perturbed lattice structure are identified using finite element analysis. Third, band gaps dependence on perturbation parameters is investigated, and neural networks are trained using finite element-based data to predict the band gaps associated with perturbation parameters. Fourth, the neural network is used to determine the perturbation design parameters (i.e., amplitude and frequency) needed to obtain a prescribed band gap. As the neural network predictions might include errors, the design parameters obtained from the neural network are considered coarse design parameters. Finally, the design parameters are refined/filtered using finite element analysis. Establishing a coarse estimate and subsequently refining it using finite element analysis reduces the number of trial-and-error finite element analysis-based iterations needed to design a lattice metamaterial with a prescribed band gap, thus reducing the design time and cost. The enumerated steps are explained in detail in the following.

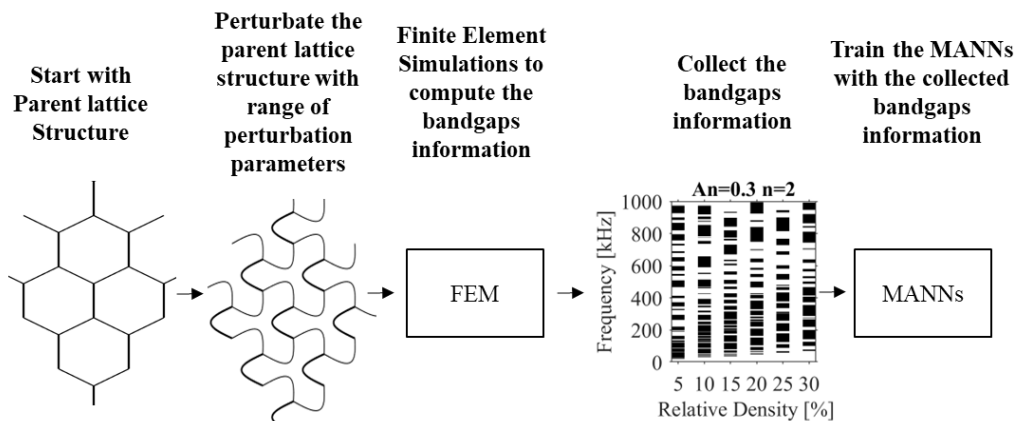


Figure 1 Schematic representation of the artificial intelligence-assisted approach for designing lattice materials with prescribed band gaps.

### 3.2. Parent Lattice Structure and Material

The parent lattice used in this work is the double-sided honeycomb shown in Figure 2. This double-sided aluminum honeycomb, which exhibits a more complex response than its single-sided honeycomb counterpart [31], is selected as it is widely used as cores in composite sandwich structures, and its fabrication process does not require expensive additive manufacturing processes. On the contrary, double-sided aluminum honeycombs are mass-produced using the conventional fabrication technique of bonding corrugated sheets [32]. Cell walls of the double-sided honeycomb lattice shown in Figure 2 are prismatic and have equal lengths ( $L$ ). However, its bonded cell walls have double the thickness ( $2t$ ) of its unbonded cell walls, as seen in Figure 2. The lattice is assumed to be made from isotropic aluminum with a modulus of 70 GPa, a Poisson's ratio of 0.33 and a density of  $2700 \text{ kg/m}^3$ . The cell walls of the lattice are assumed to have a length ( $L$ ) of 5 mm throughout this work. The in-plane thickness of the cell walls ( $t$ ) is determined from the lattice's relative density ( $\rho^*$ ), which is defined as the ratio of the density of the constituent material to the density of the lattice, using [33]

$$\rho^* = \frac{8}{3\sqrt{3}} \frac{t}{L} - \frac{4}{9} \left(\frac{t}{L}\right)^2 \quad (1)$$

Multiple relative densities are considered in this work, namely 5%, 10%, 15%, 20% and 25%, to explore the sensitivity of band gaps to relative density.

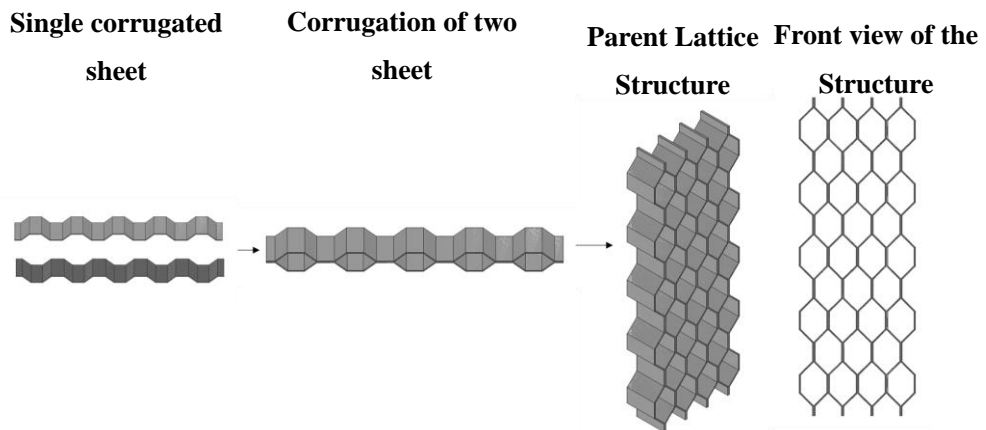


Figure 2 Parent lattice structure, showing its geometry and main features.

### 3.3. Superposing Periodic Sinusoidal Perturbation

Perturbing the cell walls of the double-sided honeycomb lattice is achieved by superposing a sinusoidal shift along the perpendicular direction to the cell walls, as seen in Figure 3. The sinusoidal shift is governed by the function

$$y(x) = A \sin \left( \frac{2\pi n}{L} x \right) \quad (2)$$

such that  $L$  is the cell wall length,  $A$  is the perturbation amplitude, and  $n$  is the number of waves per cell wall (i.e., represents perturbation frequency). As a sine function is used to drive the perturbation process, the vertices of the original lattice remain in their initial position and are not affected by the perpetuation process. The perturbation process is identically applied to all cell walls; thus, perturbed cell walls have identical perturbed geometry. The perturbation process can be applied to straight cell walls in real real-life manufacturing scenarios using bending and corrugation processes which have negligible effects on cell wall thickness. Thus, in this work, the thickness of the perturbed cell walls is assumed to be similar to that of the unperturbed cell walls.

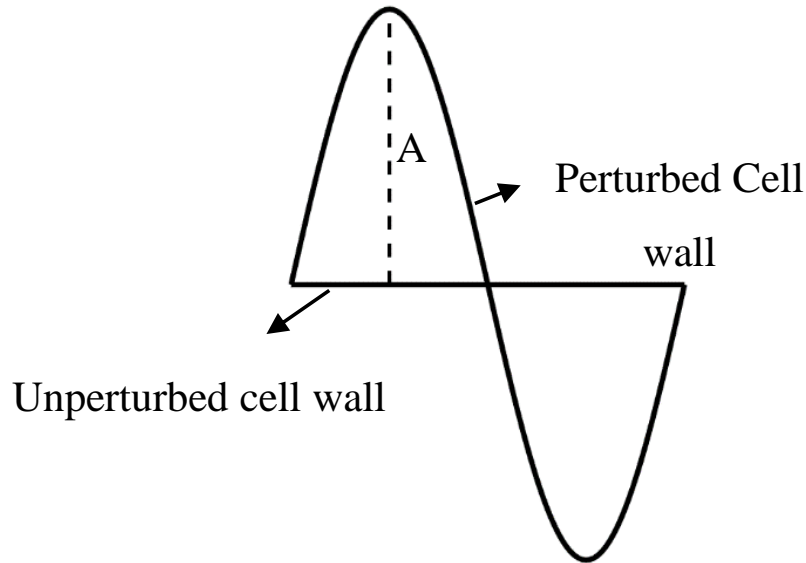


Figure 3 Schematics of the sinusoidal perturbations superposed on cell walls

Upon applying the perturbation shown in Figure 3, the length of each perturbed cell wall can be evaluated using

$$Length = \int_0^L \sqrt{dx + \left(\frac{dy}{dx}\right)^2} dx = \int_0^L \sqrt{1 + A^2 \frac{4\pi^2 n^2}{L^2} \cos^2\left(\frac{2\pi n}{L}x\right)} dx \quad (3)$$

According to Equation (3), increasing the perturbation amplitude ( $A$ ) or frequency ( $n$ ) increases the cell walls' length which, in turn, increases the mass of the perturbed lattice. The increased mass can affect the response of the perturbed lattice and complicates differentiating the effect of geometry (i.e., perturbation parameters) from that of mass on band gaps. The latter motivated rendering the perturbed cell wall length independent of perturbation parameters. Equation (3) represents a complete elliptic integral of the second kind, and its result is independent of the frequency  $n$  if the coefficient of the cosine term is independent of  $n$ . Accordingly, defining the amplitude  $A$  as follows in Equation (4) renders the length of perturbed cell walls independent of perturbation frequency [4].

$$A = \frac{A_n L}{n} \quad (4)$$

here,  $A_n$  is a unitless user-prescribed perturbation amplitude that ranges between 0 and 1. It allows for prescribing perturbation magnitude as a fraction of the unperturbed cell wall length ( $L$ ). Hereafter,  $A_n$  will be referred to as the normalized perturbation magnitude. It is important to note that the length of cell walls perturbed using Equation (1) in conjunction with Equation (4) is independent of perturbation frequency ( $n$ ) only at constant normalized perturbation amplitudes. As the thickness of perturbed cell walls is assumed to be equal to the thickness of their unperturbed counterparts, restricting the length of perturbed cell walls to be independent of perturbation frequency ensures that the mass of the perturbed honeycombs is independent of perturbation frequency at constant normalized perturbation amplitudes. This constraint allows for investigating the effect of a range of frequencies at a given normalized perturbation amplitude without considering the effect of change in mass. A wide range of perturbation frequencies and normalized amplitudes are considered to explore the potential of superposed sinusoidal perturbations in enhancing the band gaps of the double-sided honeycomb lattice. Perturbation frequencies ( $n$ ) considered include 0.5, 2, 4, 6, and 10. On the other hand, normalized perturbation amplitudes considered include 0.1, 0.2, 0.3, 0.4, and 0.5. For illustration, samples of the perturbed lattices are shown in Figure 4.

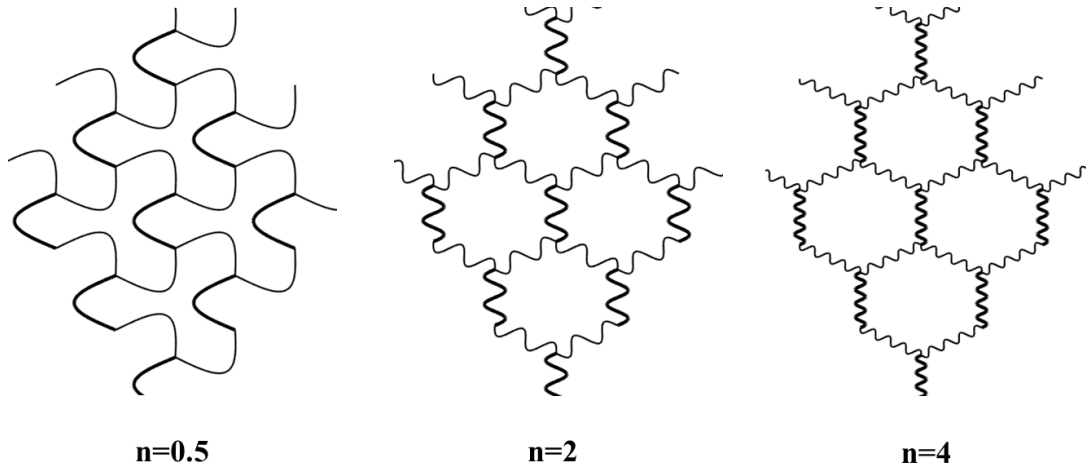


Figure 4 Examples demonstrating the geometry of the double-sided honeycomb lattice after the sinusoidal perturbation is applied ( $A_n=0.3$ )

### 3.4. Band Gap Determination Using Finite Element Analysis

Bloch wave theorem and finite element analysis are used to determine the band gaps in the parent double-sided honeycomb lattice and its perturbed counterparts. To this end, unit cell-based models, shown in Figure 5, are selected to represent the infinite periodic structures. The unit cells are chosen such that they can reproduce the geometry of their corresponding infinite structures if replicated along the basis vectors ( $\mathbf{e}_1, \mathbf{e}_2$ ).

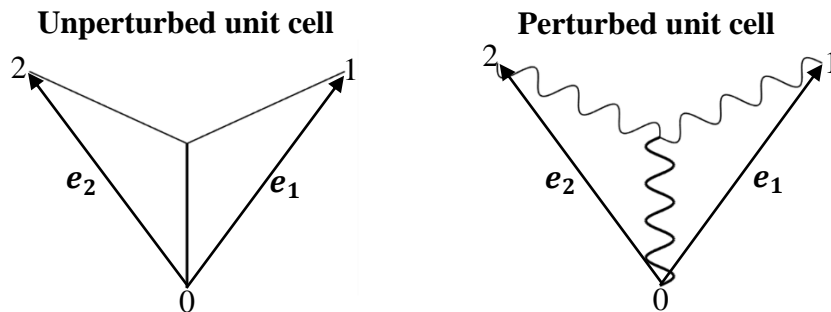


Figure 5 Schematics of the unit cells used in the finite element analysis to represent both unperturbed and perturbed honeycomb lattices.

Each unit cell is subjected to periodic boundary conditions to ensure that its behavior mimics that of its infinitely periodic parent lattice. The periodic boundary conditions are defined using Bloch wave theory following earlier efforts [11], [14]–[16], [34] that applied it to a unit cell similar to the unperturbed unit cell shown in Figure 5. According to these efforts, the periodic displacement boundary conditions that ensure the unit cell represents the behavior of its infinite parent lattice are

$$\mathbf{u}_1 = \mathbf{u}_0 e^{k_1} \quad \mathbf{u}_2 = \mathbf{u}_0 e^{k_2} \quad (5)$$

such that  $\mathbf{u}_0$ ,  $\mathbf{u}_1$  and  $\mathbf{u}_2$  are the displacement vectors at the boundary points named 0, 1 and 2 in Figure 5. On the other hand,  $k_1$  and  $k_2$  are the complex wave numbers that describe the dispersion and attenuation of waves propagating through the lattice.  $k_1$  and  $k_2$  are typically expressed in the reciprocal lattice vectors expressed ( $\mathbf{b}_1, \mathbf{b}_2$ ) as

$$\mathbf{k} = k_1 \mathbf{b}_1 + k_2 \mathbf{b}_2 = \xi_1 \mathbf{i} + \xi_2 \mathbf{j} \quad (6)$$

The reciprocal lattice vectors are related to the lattice basis vectors using  $\mathbf{b}_i \cdot \mathbf{e}_j = \delta_{ij}$  such that  $\delta_{ij}$  is the Kronecker delta. To facilitate the modelling process, the wave vector components  $k_1$  and  $k_2$  are transformed to the Cartesian coordinate system defined using the basis vectors  $\mathbf{i}$  and  $\mathbf{j}$ . Thus, any wave vector ( $\mathbf{k}$ ) can be expressed using its components  $k_1$  and  $k_2$  in the reciprocal space or  $\xi_1$  and  $\xi_2$  in the Cartesian coordinate system. For a periodic lattice, the relevant wave vector ( $\mathbf{k}$ ) values are bounded by the 1<sup>st</sup> Brillion zone [35]–[37]. For the unit cells of Figure 5, the 1<sup>st</sup> Brillion zone is shown in Figure 6

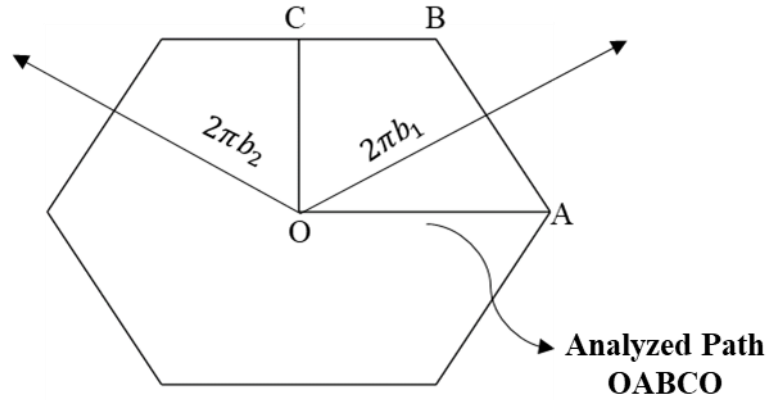


Figure 6 The 1<sup>st</sup> Brillion zone corresponding to the unit cell of Figure 5

Due to the periodic nature of the lattice, each wave vector extending beyond the 1<sup>st</sup> Brillion zone has an image inside the 1<sup>st</sup> Brillion zone. Thus, considering wave vectors beyond the 1<sup>st</sup> Brillion zone is unnecessary and redundant. The periodic boundary conditions and the 1<sup>st</sup> Brillion zone are independent of the perturbation process as the lattice basis vectors and the periodic length scale of the perturbed and unperturbed unit cells are identical.

Finite element analysis is used to apply the periodic boundary conditions defined by Equation (5) to the unit cells representing the investigated lattices (i.e., perturbed and unperturbed) and simulate their response. The commercial finite element software ABAQUS is used, and the periodic boundary conditions are implemented using the EQUATION command. Each cell wall in the unit cell is discretized using Timoshenko elements, namely B31 according to ABAQUS's terminology. Mesh sensitivity analysis showed that 50 elements per cell wall are enough to reach a mesh-independent solution for perturbed unit cells with low-frequency ranges (i.e.,  $n=0.5$  to  $n=4$ ) and 100 elements per cell wall for perturbed unit cells with high-frequency ranges (i.e.,  $n=6$  to  $n=10$ ). 50 elements per cell wall were sufficient to reach a mesh-independent solution in regular honeycombs [11], [14]–[16]. Upon applying the periodic boundary conditions, ABAQUS internally formulates the free vibration elastodynamic equilibrium equation governing the behavior of the unit cell. This equation can be described as [11], [14]–[16]

$$[\mathbf{K} - \omega^2 \mathbf{M}] \begin{bmatrix} \mathbf{u}_o \\ \mathbf{u}_i \end{bmatrix} = [\mathbf{0}] \quad (7)$$

where  $\omega$  is the Eigenfrequency,  $u_o$  is the reference node shown in Figure 5, and  $u_i$  are the non-boundary nodes of the beam elements comprising the discretized cell walls of the unit cell.  $\mathbf{K}$  and  $\mathbf{M}$  are the reduced stiffness and mass matrices which are functions of  $k_1$  and  $k_2$ . Equation (7) is an Eigenvalue problem, and solving it results in the Eigenfrequencies and Eigenmodes. To solve this equation, the values of  $k_1$  and  $k_2$  are assigned first. Subsequently, the equation is solved using ABAQUS's Lanczos solver, and all Eigenfrequencies below 1000 kHz are determined. This approach delivers the Eigenfrequencies associated with every possible wave vector value.

To determine the band gap structure of a unit cell, the wave vector  $\mathbf{k}$  is assigned values defined by the path (OABCO) shown in Figure 6. For each  $\mathbf{k}$  value on this path, all Eigenfrequencies lower than 1000 kHz are obtained using ABAQUS. As an example, the Eigenfrequencies associated with the unperturbed honeycomb lattice with a relative density of 10% are shown in Figure 7.

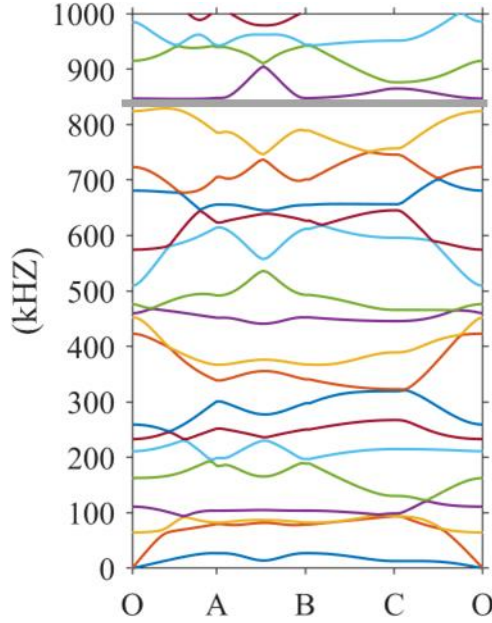


Figure 7 The band gap structure of the unperturbed honeycomb lattice with 15% relative density

Figure 7 shows the Eigenfrequencies obtained by sweeping  $k$  along the path OABCO shown in Figure 6. The figure shows a frequency zone (shaded region) that the lattice cannot support. This zone represents the lattice's frequency band gap. At 10% relative density, the unperturbed lattice shows a single narrow band gap. This behavior does not support filtering applications with different frequency ranges. However, as shown in the results section, imposing perturbations can change the observed behavior by increasing both the number of band gaps and their width.

### 3.5. Prediction of Band Gaps Using Machine Learning (ML)

The perturbation parameters considered in this study comprise five perturbation amplitudes and five perturbation frequencies. In addition, six relative densities are considered to investigate the interaction between perturbation and relative density. Thus, 150 (i.e., 5x5x6) band gap structures similar to the one presented in Figure 7 are obtained. Due to the sheer number of inputs and outputs involved, machine learning, namely artificial neural network (ANN), is used to establish a predictive relationship between the inputs (i.e., relative density, perturbation magnitude and frequency) and output (i.e., band gap data). Three key features are used to summarize the band gap data obtained for each combination of  $\rho^*$ ,  $n$ ,  $A_n$ . These are the number of band gaps, the widest band gap and the centroid of the widest band gap. These key features not only reduce the band gap data's complexity but can also be used as quantitative key

performance indicators to describe the suitability of a lattice to a particular wave isolation or filtering application.

The framework of the implemented machine-learning solution is shown in Figure 8. The framework starts by postprocessing the band gap data per combination of  $\rho^*$ ,  $n$ ,  $A_n$  and determining the corresponding key band gap features (i.e., the number of band gaps, the widest band gap and the centroid of the widest band gap). The determined key band gap features are stored in datasets that are subsequently used to train multilayer artificial neural networks (MANN). The framework utilizes a parallel MANN implementation with three MANNs: one for predicting the size of the widest band gap, one for predicting the centroid of the widest band gap, and one for predicting the number of band gaps.

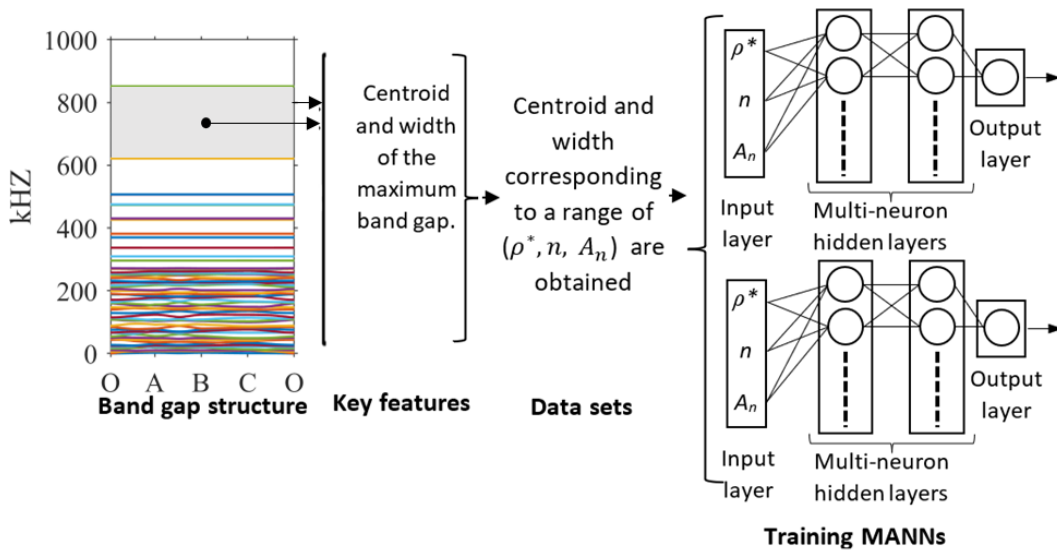


Figure 8 Schematic diagram of the implemented parallel multilayer ANNs

The architecture of the three parallel ANNs used in the framework is shown in Figure 9. This figure shows a multilayer feed-forward fully connected artificial neural network MANN. 4 layers are used per MANN. The first layer is the input layer and has three inputs, which are the relative density, the perturbation frequency, and the perturbation amplitude. The second and third layers are hidden layers and consist of multiple neurons. The fifth layer is the output layer and consists of a single neuron whose activation function provides the prediction.

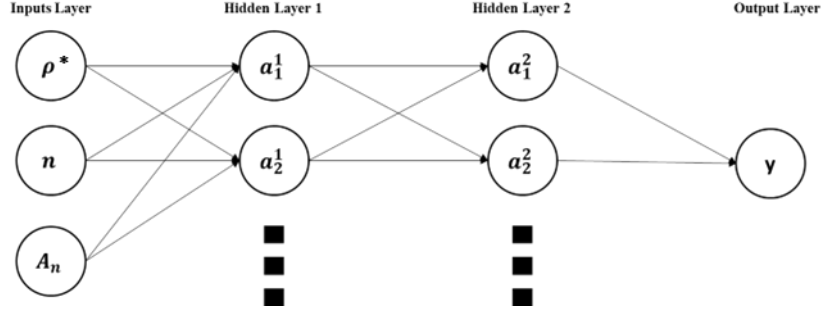


Figure 9 Feed forward multilayer MANN architecture

The activation functions of the neurons comprising the hidden layers are sigmoidal functions and are represented as [30], [38].

$$f(\eta) = \frac{1}{1 + e^{-\eta}} \quad (8)$$

where  $\eta$  is the corresponding weighted input for each neuron which is defined as  $\eta = wp + b$ . Here,  $w$  is the weight,  $p$  is the input value, and  $b$  is the bias. The activation function chosen for the output layer is the pure-line function which is defined as  $f(\eta) = \eta$ . The number of neurons comprising the hidden layers is optimized based on the combination that enhances the accuracy of the MANNs.

The backpropagation supervised learning approach is adopted to find the optimal set of the neural network weights. The backpropagation method is used to train the weights of the MANNs by utilizing the datasets (of size  $s \times 4$ ) created using the key features of the band gap structures. Error gradient is introduced for the backpropagation such that the difference between the new and old weights during an iteration can be represented as

$$\Delta w_{jk} = \alpha \times y_j \times \delta_k(p) \quad (9)$$

where  $\Delta w_{jk}$  is the difference between the new and old weights,  $y_j$  the output layer in neuron  $j$  and  $\delta_k(p)$  is the error gradient at neuron  $k$  that corresponds to the output layer at iteration ( $p$ ). The error gradient  $\delta_k(p)$  is represented as:

$$\delta_k = \frac{\partial y_k}{\partial \zeta_k} \times e_k(p) \quad (10)$$

where  $y_k$  is the output layer in neuron  $k$ ,  $\eta_k$  is the weighted input in neuron  $k$ , and  $e_k(p)$  is the error between the output layer prediction ( $y_k$ ) and the actual value ( $y_{ak}$ ) from the

dataset. This procedure is done iteratively until attaining a predefined threshold for the least mean squared error cost function (MSE) defined in Equation (11)

$$MSE = \frac{1}{s} \sum_i^s (y_{ai} - f(\eta_i))^2 \leq \varepsilon \quad (11)$$

where  $y_{ai}$  is the desired output value and  $y_i = f(\eta_i)$  is the output value acquired by the output layer in the MANN. Once the predefined threshold ( $\varepsilon$ ) is reached, the final set of weights of the MANN in each layer presents the nonlinear mapping between the network inputs and outputs. The block diagram shown in Figure 10 summarizes the training process for the MANNs using a supervised learning approach. The training of the MANNs was performed using the neural network toolbox MATLAB.

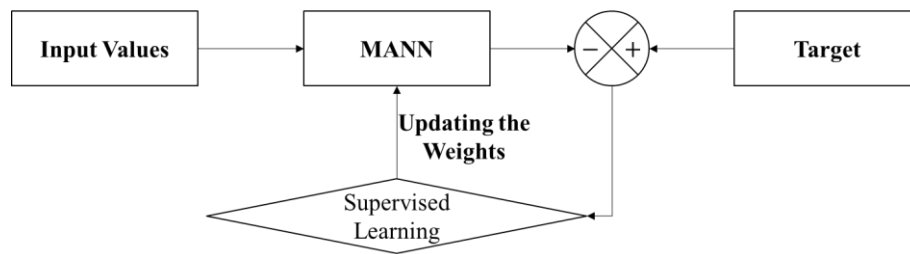


Figure 10 Block diagram of the training process for MANN using supervised learning

## Chapter 4. Results

### 4.1. Verification of The Finite Element-Approach and Its Implementation

The finite element-based approach used in this work and its implementation in ABAQUS were verified by accurately reproducing the eigenfrequencies of a well-characterized lattice in literature. To this end, the eigenfrequencies of a single-sided honeycomb lattice identical to that used in reference [11] were determined using the finite element methodology described above. The lattice used had a cell size of 5 mm, a constituent material stiffness and density of 70 GPa and  $2700 \text{ kg/m}^3$ , respectively, and a relative density of 5%, 10%, 15% and 30%. As shown in Figure 11, the resulting eigenfrequencies are identical to those reported in reference [11]. Reproducing the exact results reported in the literature for different relative densities validates this work's finite element-based methodology and implementation.

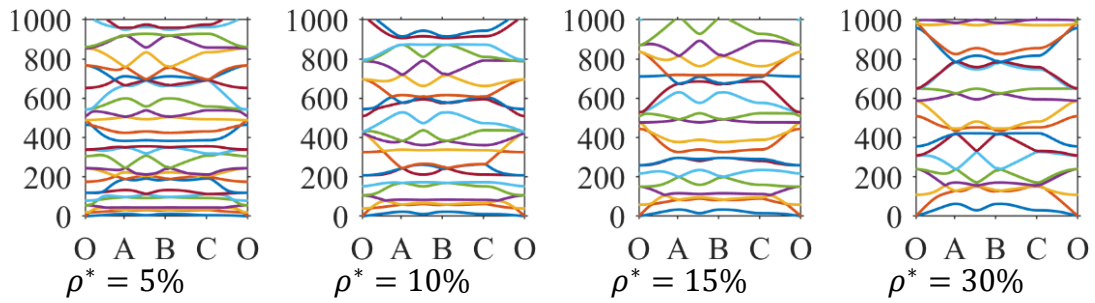


Figure 11 Eigenfrequencies of single-sided aluminum honeycomb hexagonal lattice with the relative densities of 5%,10%,15%, and 30%. The analyzed lattice and shown results are identical to those presented in reference [11].

### 4.2. Bandgaps of The Unperturbed Double-Sided Honeycomb

To establish a benchmark that facilitates measuring the effect of imposed sinusoidal perturbations, the eigenfrequencies and bandgaps, in the 1000kHz range, of the unperturbed double-sided honeycomb lattice described in the Methodology section were determined at the relative densities of 5%, 10%, 15%, 20%, 25%, 30%. The resulting eigenfrequencies and bandgaps are shown in Figure 12. This figure shows that the unperturbed double-sided honeycomb does not exhibit bandgaps at small relative densities (i.e., 5% and 10%) and exhibits a single narrow bandgap at the relative densities of 15%, 20%, 25%, and 30%. Hence, the unperturbed double-sided lattice is not suitable for wave control and filtering applications. However, this unfavorable wave

application behavior can be improved by incorporating perturbations since they would substantially increase the number and widths of band gaps as shown in the next section.

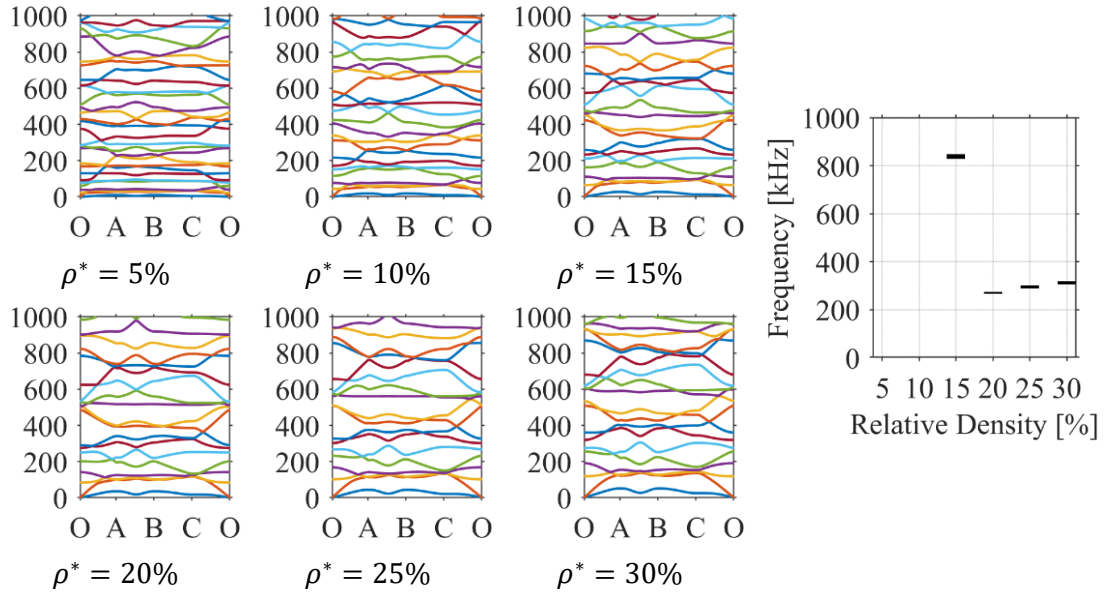


Figure 12 Eigenfrequencies of double-sided aluminum honeycomb hexagonal lattice with the relative densities of 5%, 10%, 15%, 20%, 25%, and 30%.

### 4.3. Band Gaps of The Perturbed Double-Sided Honeycomb

The Eigenfrequencies and band gaps of the perturbed double-sided honeycomb lattices in the 1000kHz range were obtained for all combinations resulting from the selected perturbation magnitudes (0.1, 0.2, 0.3, 0.4, 0.5), perturbation parameters (0.5,2,4,6,10), and relative densities (5%, 10%, 15%, 20%, 25%, 30%). The band gaps of all analyzed perturbed cases are shown in Figure 13. Due to the large number of cases analyzed (i.e., 125 cases), the eigenfrequency plots of the perturbed cases are not shown; only the resulting band gap structures are shown.

Perturbations, as seen in Figure 13, significantly increased the number and size of the double-sided honeycomb band gaps; thus, they transformed a one-band gap structure into a band gap-rich structure. This transformation supports the hypothesis that perturbations can help design metamaterials with prescribed band gap properties. Insights into the effectiveness of incorporating perturbations as an approach for creating functional frequency band gaps can be inferred from Figure 13. Effectiveness here can be defined in terms of the ability of perturbations to generate a band gap, though by different perturbation parameters, at every frequency in the range of 0 to 1000kHz. In

other words, effectiveness can be defined in terms of the ability of the different perturbations to collectively block all the frequencies in the range of 0~1000kHz. Superposing all band gaps presented in Figure 13 shows that the imposed perturbations can collectively generate a band gap at every frequency from 100kHz to 1000kHz. Thus, for every frequency in this range, one can find a perturbation scenario that will result in a band gap. This result demonstrates the efficiency of incorporating perturbations to create functional band gaps at application-specific frequencies.

Although incorporating perturbations can generally develop more band gaps and increase their widths, the band gap-enhancing effect of perturbations is not easily predictable, as demonstrated by Figure 13. The effect of perturbation parameters on band gaps seems complex, with nonlinear and non-monotonic patterns. To demonstrate the complex effect of perturbation frequency, consider, for example, the case with the perturbation magnitude ( $A_n$ ) of 0.1. Low perturbation frequency ( $n=0.5$ ) resulted in many narrow band gaps at all relative densities considered. Increasing the perturbation frequency ( $n$ ) to 2, in general, increased the number of band gaps and increased the number of band gaps with larger bandwidths. However, increasing the perturbation frequency further, to 6 or 10, decreased the number of band gaps but increased the widths of the bands exhibited at low relative densities. Moreover, at the highest relative densities considered, a single band gap was observed, which is similar to the behavior of the unperturbed case. Similarly, to demonstrate the non-intuitive and non-monotonic effect of perturbation magnitudes at a constant frequency, consider the case with a perturbation frequency of  $n=0.5$ . Increasing the perturbation magnitude from 0.1 to 0.2 and from 0.2 to 0.3 resulted in a rapid increase in the number of band gap frequencies; however, increasing the perturbation magnitude from 0.3 to 0.4 resulted in a minor increase in the number of band gaps. Moreover, few band gaps disappeared with increasing perturbation frequencies. The examples above show that the individual effects of perturbation frequency and perturbation amplitude are non-monotonic, nonlinear, and not systematically predictable without using experimentation or conducting detailed finite element simulations. This complex behavior would hinder using perturbations in designing metamaterials with prescribed band gap behavior. The complexity of the data shown in Figure 13 motivates using a data-driven approach to systematically predict the band gap characteristics corresponding to any combination

of perturbation parameters at any relative density. To this end, machine learning, namely artificial neural networks, is used.

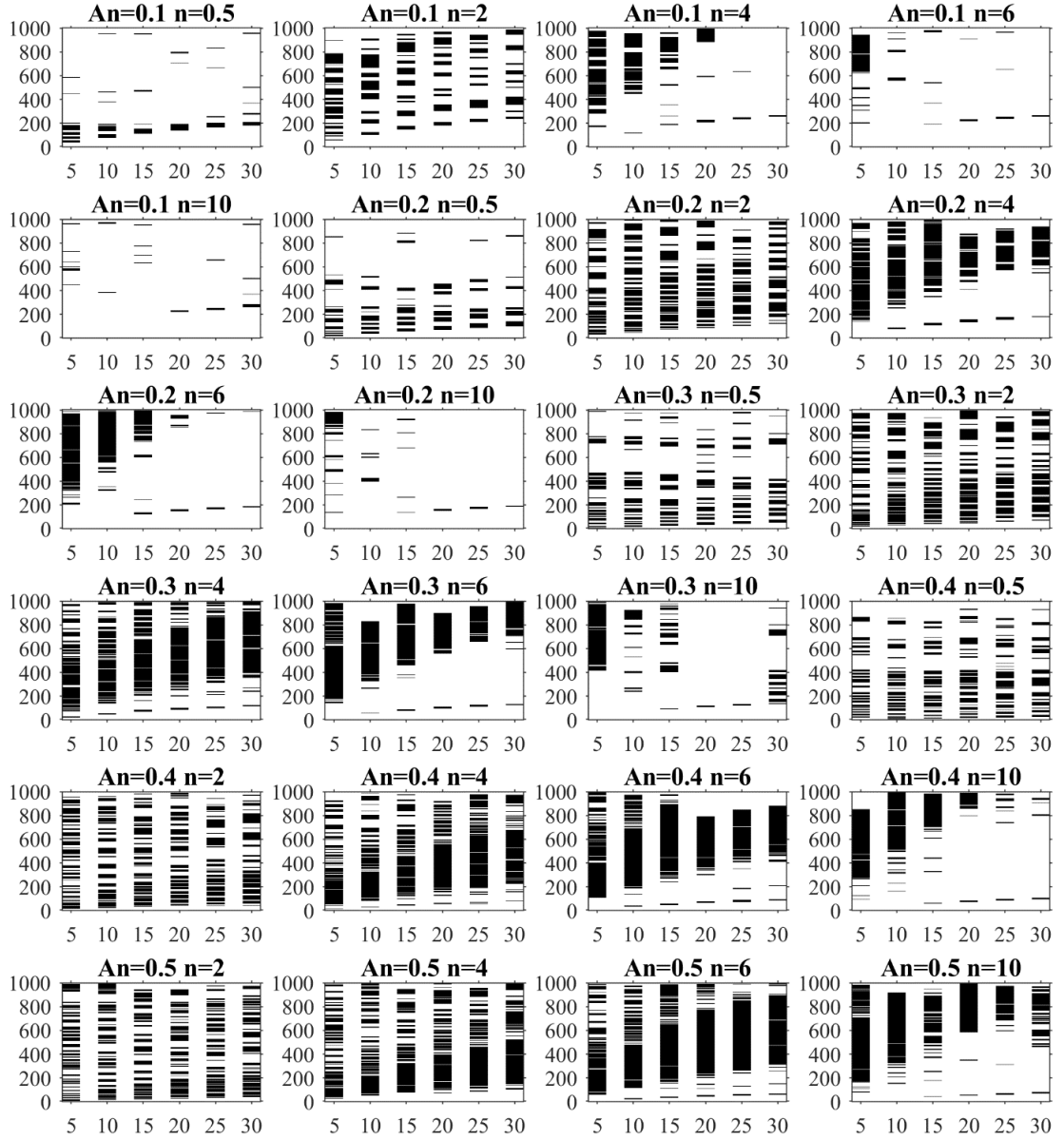


Figure 13 Band gaps of perturbed double-sided aluminum honeycomb hexagonal lattice, showing the band gaps for the perturbation amplitudes of 0.1,0.2,0.3,0.4 and 0.5; perturbation frequencies of 0.5, 2, 4, 6 and 10 (cycles); and relative densities of 5%, 10%, 15%, 20%, 25%, and 30%.

To facilitate using machine learning methods, the data presented in Figure 13 is summarized using key frequency band gap features observed at every perturbation scenario. These are the number of band gaps, the maximum band gap width, and the centroid of the band gap with the maximum width. Figure 14 to Figure 19 show the key frequency band gap features corresponding to the different perturbation parameters used at the relative densities of 5%, 10%, 15%, 25%, and 30%, respectively. These

figures show that the perturbation parameters result in different band gap characteristics at each relative density.

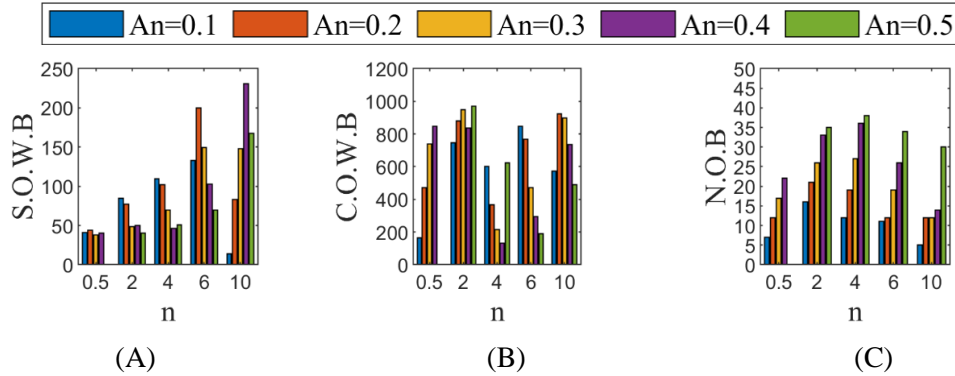


Figure 14 Key band gap features at 5% relative density, showing (A) the size of widest band gap (S.O.W.B) in kHz, (B) its centroid (C.O.W.B) in kHz and (C) the number of band gaps.

At 5% relative density, according to Figure 14, the perturbation parameters  $An=0.4$  and  $n=10$  result in the widest band gap exhibited at this relative density. This band gap has a width of 230.53 kHz, a centroid of 736.5 kHz, and is the largest observed at all relative densities and considered perturbation parameters. This figure shows that the maximum number of band gaps and the widest band gap do not necessarily occur at the same perturbation parameters. At 5% relative density, the maximum number of band gaps, 38, is observed at  $An=0.5$  and  $n=4$ , which are different from the parameters resulting in the widest band gap at the same relative density.

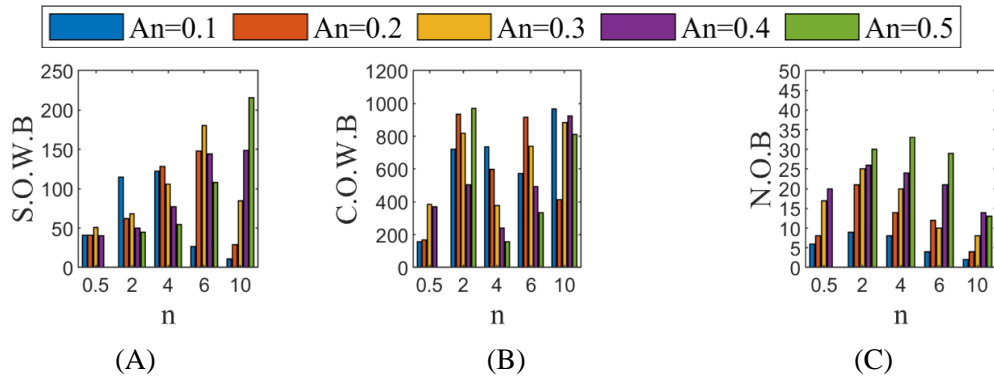


Figure 15 Key band gap features at 10% relative density, showing (A) the size of widest band gap (S.O.W.B) in kHz, (B) its centroid (C.O.W.B) in kHz and (C) the number of band gaps.

At the relative density of 10%, according to Figure 15, the widest band gap, which has a width of 215.83 kHz and a centroid of 810.07 kHz, is observed at a different set of perturbation parameters, namely  $An=0.5$  and  $n=10$ , than those associated with the

widest band gap at 5% relative density. However, similar to the 5% relative density case, at the relative density of 10%, the perturbation parameters ( $An=0.5$  and  $n=10$ ) resulting in the maximum number of band gaps do not coincide with those resulting in the widest band gap ( $An=0.5$  and  $n=4$ ).

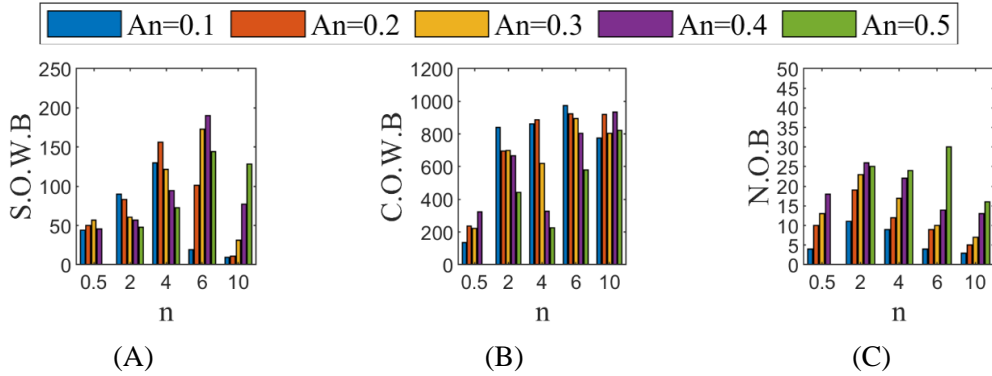


Figure 16 Key band gap features at 15% relative density, showing (A) the size of widest band gap (S.O.W.B) in kHz, (B) its centroid (C.O.W.B) in kHz and (C) the number of band gaps.

Increasing the relative density to 15%, as seen in Figure 16, further reduces the widest obtainable band gap. This band gap, which has a size of 189.88 kHz and a centroid of 802.45 kHz, is observed at the perturbation parameters of  $An=0.4$  and  $n=6$ . These parameters are different from those resulting in the widest band gap at both 5% and 10% relative densities. Although the largest band gap at 15% relative density is narrower than the widest band gaps observed at 5% and 10% relative densities, it covers the frequency range between them. This non-monotonic behavior is rather difficult to predict. Figure 16 shows a secondary substantially large band gap at the perturbation parameters of  $An=0.5$  and  $n=6$ . This band gap, which has a size of 144 kHz and a centroid of 581.21 kHz, is smaller but comparable in size to the one observed at  $An=0.4$  and  $n=6$ . The perturbation scenario resulting in the second widest band gap at 15% relative density also results in the maximum number of band gaps (i.e., 30).

At 20% relative density, the band gap with maximum width is associated with the perturbation parameters of  $An=0.5$  and  $n=6$ , as seen in Figure 17. The band gap has a size of 181.47 kHz, and it is the smallest bandgap among those classified as widest at their respective relative densities. The widest bandgap at 20% relative density covers a lower frequency range than that covered by the widest bandgap at the relative densities of 5%, 10% and 15%. The maximum number of band gaps observed at 20% relative density (28 bands) is comparable to that observed at 5%, 10% and 15% relative

densities; however, it appeared at a different set of perturbation parameters, namely  $An=0.5$  and  $n=2$ .

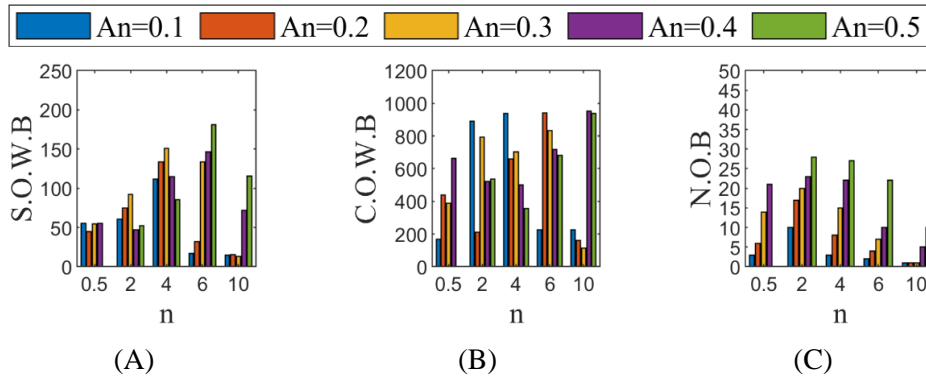


Figure 17 Key band gap features at 20% relative density, showing (A) the size of widest band gap (S.O.W.B) in kHz, (B) its centroid (C.O.W.B) in kHz and (C) the number of band gaps.

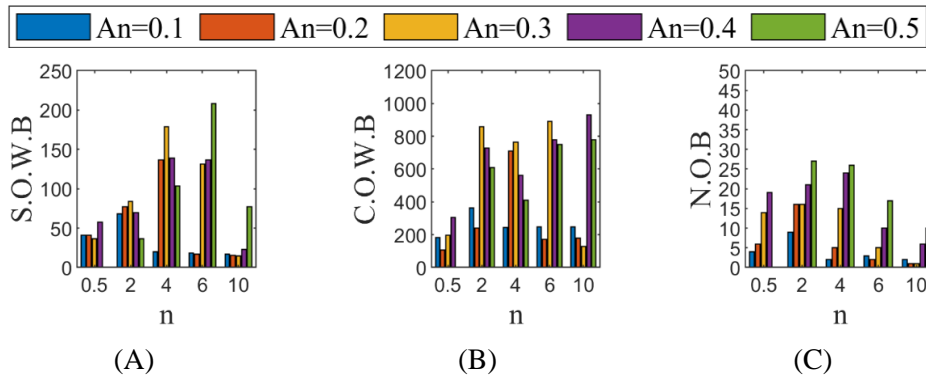


Figure 18 Key band gap features at 25% relative density, showing (A) the size of widest band gap (S.O.W.B) in kHz, (B) its centroid (C.O.W.B) in kHz and (C) the number of band gaps.

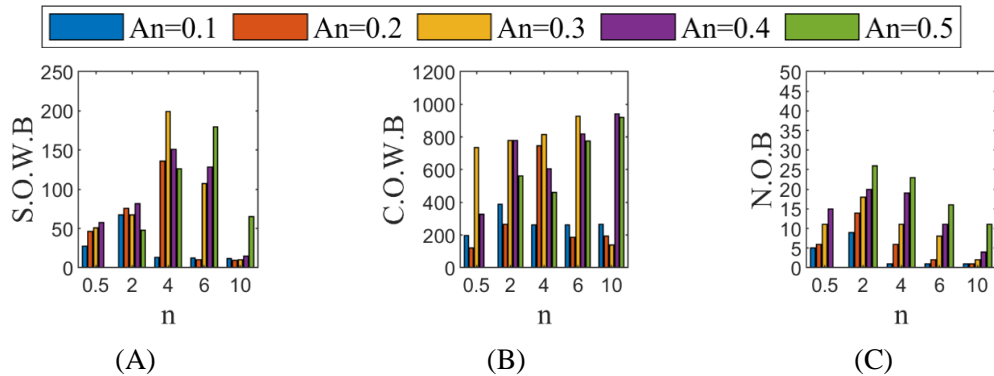


Figure 19 Key band gap features at 30% relative density, showing (A) the size of widest band gap (S.O.W.B) in kHz, (B) its centroid (C.O.W.B) in kHz and (C) the number of band gaps.

Figure 18 presents the key band gap features at the relative density of 25%. Comparing this figure to Figure 17 shows that perturbation parameters resulting in the widest band gap and maximum number of gaps at 25% relative density are identical to their

counterparts at 20% relative density. However, compared to the 20% relative density case, the band exhibited at 25% relative density, which has a width of 207.84 kHz, is wider. On the other hand, the maximum number of band gaps at 20% and 25% relative densities were very comparable, 28 bands for the former and 27 bands for the latter.

At the highest relative density considered, 30%, as seen in Figure 19, the widest band gap, 199.37 kHz in width, is observed at the perturbation parameters  $A_n=0.3$  and  $n=4$ . Comparing this to the results at the other relative densities highlight a trend in which the widest band gaps at higher relative densities are observed at smaller perturbation frequencies and magnitudes. Also, at higher relative densities, the widest band gap decreases in size. However, with respect to the maximum number of band gaps, the 30% relative density case almost mirrored the behavior of the 25% and 20% relative density cases. It exhibited a comparable number of maximum band gaps, 26, at the same perturbation parameters that resulted in the maximum number of band gaps at 20% and 25% relative densities.

Results summarizing the key band gap features indicate that perturbations are more efficient in generating functional band gaps, larger in number and width, at lower relative densities. Moreover, results followed a non-monotonic and complex pattern that renders predicting them without machine learning difficult.

#### **4.4. MANNs Implementations for The Three Key Aspects:**

As demonstrated in the diagram of the proposed framework in Figure 8, parallel feed-forward multilayer artificial neural networks (MANNs) are implemented for predicting the three key bandgap features, a MANN for each feature. The inputs of the MANNs are relative density, perturbation amplitude ( $A_n$ ), and perturbation frequency represented by the number of perturbation waves per ligament ( $n$ ). Each of the three MANNs has two hidden layers whose optimal number of neurons is determined using sensitivity analysis. Data presented in Figure 14 to Figure 19 are used to train and optimize the MANNs. Collected data are divided into three sets: 80% for training, 10% for testing and 10% for validation.

The first MANN models the bandgap with the maximum width formed at each combination of  $\rho^*$ ,  $A_n$  and  $n$ . The optimal configuration for this MANN's is obtained when its first and second hidden layers have seven and six neurons, respectively. Figure

20 shows the performance (i.e., mean square error (MSE) defined by Equation (11)) and regression plot (i.e., describes the correlation between the output and target) of the optimal MANN. Both performance (MSE of 0.0067 after 11 epochs) and regression plot (with a good fit,  $R^2$  of 0.97) suggest the proposed MANN has a promising predictive ability. The accuracy of the proposed MANN in predicting the maximum bandgap width is measured by comparing the MANN predictions to the finite element results. The proposed MANN has a maximum accuracy of 99.94% and a minimum accuracy of 78.35%. The minimum accuracy is associated with the parameters of  $\rho^* = 20\%$ ,  $A_n=0.1$  and  $n=10$ . To represent the MANN's predicting error in a compact manner, the mean error measure is computed by averaging the MANN prediction error (i.e., magnitude) for all  $A_n$  values (i.e., 0.1, 0.2, 0.3, 0.4 and 0.5) at each combination of  $\rho^*$  and  $n$ . The resulting mean error values are presented in Table 1. This table shows that the minimum mean error is observed at  $\rho^* = 15\%$  and  $n=0.5$ , while the maximum mean error is observed at  $\rho^* = 20\%$  and  $n= 4$ . Moreover, the maximum mean error is less than half of the maximum error corresponding to the 78.35% accuracy. The latter indicates that the MANN prediction error is small in most cases.

The second MANN models the number of band gaps formed at each combination of  $\rho^*$ ,  $A_n$  and  $n$ . This MANN's optimum configuration has two hidden layers. The first has seven neurons, while the second has five neurons. The MANN's performance (MSE plot) and regression plots are shown in Figure 21. Both performance (MSE of 0.0062 after 9 epochs) and regression plot (with a good fit,  $R^2$  of 0.98) suggest the proposed MANN has a promising predictive ability. The accuracy of the proposed MANN is computed by comparing its predictions with finite element results. It has a maximum accuracy of 99.4% and a minimum accuracy of 79.68%. The minimum accuracy is observed at the input parameters of  $\rho^* = 5\%$ ,  $A_n=0.2$  and  $n=10$ . The proposed MANN for modeling the number of band gaps formed has relatively the same accuracy range associated with the MANN proposed for modeling the maximum band gap width. Table 2 presents the mean error attained while utilizing the proposed MANN for predicting the number of band gaps formed due to imposing sinusoidal perturbations. The minimum and maximum mean error corresponding to predicting the number of band gaps at different  $A_n$  values are exhibited at  $\rho^* = 30\%$ ,  $n=4$  and  $\rho^* = 5\%$ ,  $n=10$ , respectively.

The third MANN predicts the centroid of the band gap with the maximum width. The optimum configuration of the latter MANN is comprised of two hidden layers. The first has six neurons and the second has three neurons. The performance (MSE plot which shows a minimum value of 0.03 after 10 epochs) and regression plot (which demonstrates an acceptable fit with an  $R^2$  value of 0.81) of the proposed MANN are shown in Figure 22. The performance of the proposed MANN for predicting the centroid of the band gap with the maximum width showed lower accuracy than the MANNs proposed for predicting the maximum band gap width and maximum number of band gaps. This inferior behavior is due to the complex and fluctuating pattern followed by the centroid of the band gap with the maximum width. Table 3 presents the proposed MANN's mean error in predicting the centroid of the band gap with maximum width.

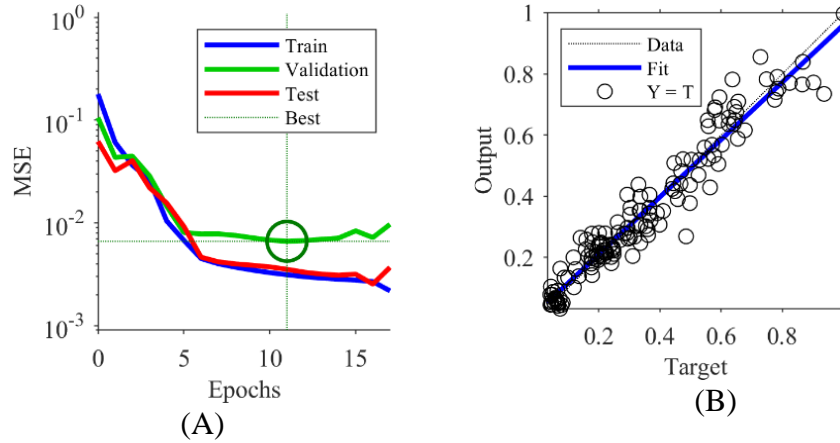


Figure 20 Performance of the MANN proposed for predicting the maximum band gap width exhibited by the sinusoidally perturbed hexagonal honeycomb. A) shows MSE plot and B) shows the regression plots.

Table 1 The mean error (%) of the MANN proposed for predicting the maximum band gap width exhibited by the sinusoidally perturbed hexagonal honeycomb. Table shows the effect of relative density ( $\rho^*$ ) and perturbation frequency ( $n$ ). The mean error (%) is compute by averaging the errors corresponding to a range of perturbation amplitudes ( $A_n$ ).

$\rho^*$	Perturbation frequency ( $n$ )				
	0.5	2	4	6	10
	Mean Error (%)				
5%	3.79	3.6	3.29	4.37	4.95
10%	2.5	3.6	2.96	2.7	4.97
15%	1.69	3.33	7.23	2.90	2.51
20%	3.01	4.43	9.917	9.12	3.46
25%	5.45	2.927	4.49	7.69	2.54
30%	3.6	6.50	5.19	4.4	2.24

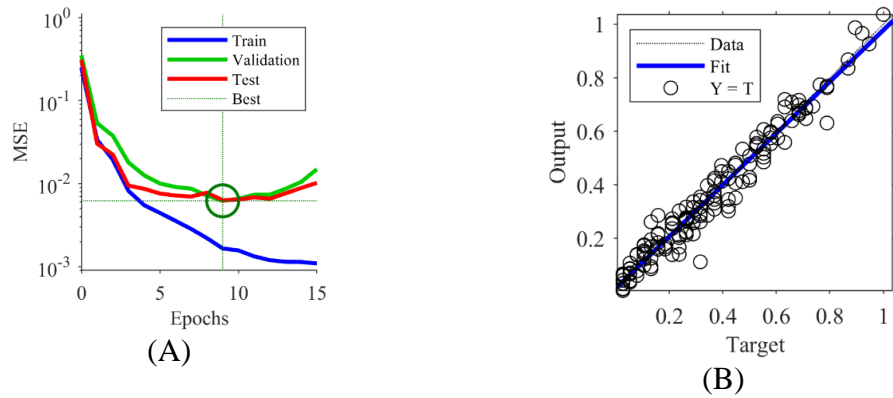


Figure 21 Performance of the MANN proposed for predicting the number of band gaps exhibited by the sinusoidally perturbed hexagonal honeycomb. A) shows MSE plot and B) shows the regression plots.

Table 2 The mean error (%) of the MANN proposed for predicting the number of bandgaps exhibited by the sinusoidally perturbed hexagonal honeycomb. Table shows the effect of relative density ( $\rho^*$ ) and perturbation frequency ( $n$ ). The mean error (%) is compute by averaging the errors corresponding to a range of perturbation amplitudes ( $A_n$ ).

$\rho^*$	Perturbation frequency ( $n$ )				
	0.5	2	4	6	10
	Mean Error (%)				
5%	2.25	3.10	3.36	5.62	6.76
10%	2.74	3.61	4.80	4.50	3.16
15%	3.94	4.11	3.82	5.35	4.39
20%	3.56	4.69	4.20	3.26	4.96
25%	2.97	5.95	3.70	2.65	1.88
30%	5.91	5.53	1.67	2.75	2.64

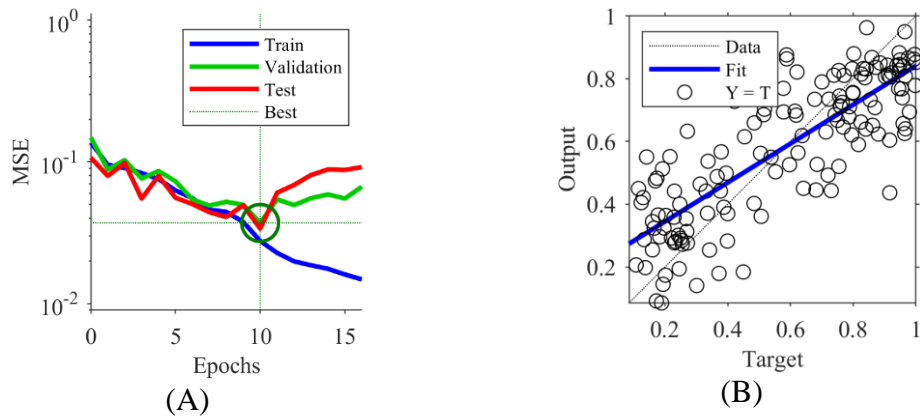


Figure 22 Performance of the MANN proposed for predicting the centroid of the band gap with maximum width. A) shows the MSE plot and B) shows the regression plots.

Table 3 The mean error (%) of the MANN proposed for predicting the centroid of the band gap with maximum width in the sinusoidally perturbed hexagonal honeycomb. Results show the effect of relative densities and perturbation frequency (n). The mean error (%) is compute by averaging the errors corresponding to a range of perturbation amplitudes (An).

$\rho^*$	Perturbation frequency (n)				
	0.5	2	4	6	10
	Mean Error (%)				
5%	17.14	7.47	10.93	8.13	11.04
10%	19.59	19.33	6.03	13.38	15.02
15%	8.96	16.81	4.79	11.72	12.05
20%	15.34	22.06	13.90	16.41	16.81
25%	12.87	14.92	18.70	12.27	14.30
30%	18.54	13.67	15.30	11.91	15.24

Again, the mean error is computed by averaging the MANN's prediction errors for all An values at each combination of  $\rho^*$  and n. The minimum mean error in predicting the centroid of the maximum band gap is observed at  $\rho^* = 15\%$  and n=4. On the other hand, the maximum mean error is observed at  $\rho^* = 20\%$  and n=2.

The results above show that the performance of the MANNs in predicting the key band gap features varies depending on the feature, perturbation parameters and relative density. The MANNs are more accurate at predicting the number of band gaps and maximum band gap width than at predicting the centroid of the maximum band gap. According to the mean error tables, the proposed MANNs are, on average, at least 90% and 94.05% accurate in predicting the maximum band gap width and number of band gaps, respectively. On the other hand, at predicting the centroid of the maximum band gap, the proposed MANN is, on average, at least 77.94% accurate. Accordingly, the MANNs predict the maximum band gap in a slightly shifted position. As the maximum band gaps are wide and the error in centroid is reasonable, the predicted band gaps significantly but not fully overlap with the actual band gaps in most cases. Therefore, the predictions of the MANNs can be efficient in assisting the design process of metamaterials with prescribed band gaps.

## Chapter 5. Discussion

The main objective of this work is to demonstrate the potential of imposing perturbations as a systematic process for designing metamaterials with prescribed functional band gaps. As mentioned in the introduction, this systematic process would provide a paradigm shift in the field for two reasons. First, currently designing metamaterials that exhibit unique band gaps is based on trial-and-error approaches in which a lattice is selected, analyzed computationally or experimentally, and its band gaps within a frequency range of interest are determined. If its response is incompatible with the required behavior, a different lattice or constituent material is analyzed. Such efforts have been applied to many lattices [1]–[4]. Collectively these efforts form a database from which one can choose the lattice needed based on its band gap characteristics. However, this route is expensive from a design perspective and results in lattice structures with very complex geometries whose fabrication requires expensive additive manufacturing processes. The highlighted difficulties hindered the implementation of the developed lattice metamaterials in applications. On the other hand, the systematic approach presented in this work adopts the common hexagonal lattice which can be made using simple corrugation-based processes [32]. Fabricating the perturbed honeycomb lattices is more complex than regular hexagonal lattices. However, it is possible using modified corrugation-based processes that incorporate perturbations in the molds used to produce the corrugations. Accordingly, the systematic approach allows conventional machining-based fabrication processes to fabricate metamaterials with prescribed band gaps. Using corrugated lattices is more practical than using complex geometries and additive manufacturing.

Second, imposing perturbations does not alter the topology of the lattice; it only alters its morphology. Accordingly, imposed perturbations can be considered morphological changes leading to different behaviors. The latter provides an opportunity for designing metamaterials with adaptive behaviors that change in response to an external trigger. To this end, the lattice would be made from an active constituent material (e.g., 4D printed lattice [39], [40], and perturbations would be imposed by controlling the active constituent material using an external trigger (e.g., heat). Subsequently, different perturbations can be imposed by varying the level of the trigger, allowing for realizing a wide range of adaptive or tunable band gaps using a single lattice.

Results confirmed that imposing perturbation can be a very effective approach for designing metamaterials with prescribed functional band gaps. This conclusion is based on two important aspects. First, results showed that perturbations transformed a simple lattice with a single narrow band gap (order of 1000kHz in width) into a lattice that exhibits multiple wide band gaps (reaching an order of 200kHz in width). This result confirmed that a rich band gap behavior could be created by imposing perturbations on a simple lattice, such as the hexagonal honeycomb used in this work. Creating numerous band gaps increases the probability of having a band gap in the region of interest. Second, and more importantly, results showed that varying the perturbation parameters and the lattice's relative density resulted in a band gap at almost every frequency ranging from 0 kHz to 1000 KHz. Imposing perturbations transforms the design problem into a parameter selection problem in which one needs to select the perturbation parameters and relative density needed to obtain a desirable band gap behavior. Accordingly, imposing perturbations is a very effective approach for designing metamaterials with prescribed band gap behavior, and it allows for using simple lattice structures, such as the honeycomb used in this work.

The major drawback of creating band gaps using perturbations is that the effect of perturbations on band gaps is complex and only readily predictable using detailed finite element simulations. The number of band gaps, their width, and covered range exhibited non-monotonic and nonlinear dependence on perturbation parameters and relative density. Nevertheless, results demonstrated few repeating patterns. Perturbations are more efficient in creating band gaps at lower relative densities. Higher efficiency is represented by a higher number of band gaps and wider band gaps. Bands with the largest widths are narrower and appear at lower perturbation parameters at larger relative densities. The latter results are consistent with the literature highlighting the ability of lattices with higher porosities to exhibit more dispersive properties and gaps [11].

The complexity of the relationship between band gap characteristics and perturbation parameters motivated using machine learning to model it. Accordingly, band gap characteristics, represented by the three key features: the number of band gaps as well as the width and centroid of the widest band gap, were modeled by multilayer artificial neural networks (MANNs). Three parallel MANNs were proposed, and results

demonstrated their ability to accurately predict the number of band gaps (94% accurate on average) and the width of the widest band gap (90% accurate on average) at each perturbation scenario and relative density. However, the MANNs ability to predict the centroid of the widest band gap was less accurate (77.94% accurate on average). The latter causes the MANNs to predict the widest band gaps at a shifted location. However, as the widest bandgaps are wide and errors associated with their predicted centroid do not grossly change their location, the predicted band gaps partially overlapped with the actual band gaps in most cases. Therefore, the proposed MANNs can be very practical in assisting the design process of metamaterials with prescribed band gaps. For instance, they can be used to determine the approximate perturbation parameters and relative density needed to obtain a specific band gap behavior. The parameters can be subsequently refined using finite elements. This process is illustrated in the following design case study.

This case study used perturbations to create a metamaterial with a band gap between 575 kHz and 625kHz. The proposed MANNs were used to determine the course design parameters that can deliver a band gap structure in which the widest band gap has a width of 50kHz and a centroid of 600 kHz. The MANNs were used iteratively to determine the 5 design points that can deliver the closest behavior to the required one. The  $\rho^*$ ,  $An$ ,  $n$  parameters of the determined design points, which were determined in a few seconds, are listed in Table 4. The actual band gap width and centroid corresponding to the selected 5 design scenarios were determined using the finite element-based approach presented in the Methodology section. Finite element predicted values are presented in Table 4. Finite element results demonstrate that frequency band gaps corresponding to the parameters of the first 3 cases overlaps with band gap required (575 ~ 625 kHz). To demonstrate this overlap, Figure 23 compares, for design configuration number 2, the widest band gap predicted by the MANNs with that predicted by the finite element analysis. This figure also shows the unit cell corresponding to design configuration 2. Figure 23 shows the significant overlap between the MANNs' predicted response and the finite element calculated response. Accordingly, by assisting the design process with artificial intelligence, only five design cases were analyzed via finite element to determine the design parameters needed to obtain the required frequency band gap. The latter demonstrates the MANNs

utility in reducing the computational costs associated with designing metamaterials with specific band gaps.

Table 4 MANNs' predicted perturbation parameters corresponding to the frequency band gap between 575 kHz and 625kHz.

Design point	MANNs Estimated					Predicted via FE Simulations	
	$\rho^*$	$A_n$	$n$	Maximum Band gap width (kHz)	Centroid of band gap with Maximum width (kHz)	Maximum Band gap width (kHz)	Centroid of band gap with Maximum width (kHz)
1	27.5	0.44	1	50.27	550.25	70.94	612.26
2	26.25	0.44	1	49.62	549.46	74.22	599.43
3	12.5	0.24	1.5	54.08	595.93	69.21	605.00
4	22.5	0.4	1	50.50	550.36	81.0	639.40
5	8.75	0.36	0.5	45.08	550.40	45.94	675.86

Perturbated unit cell



Band-Structure

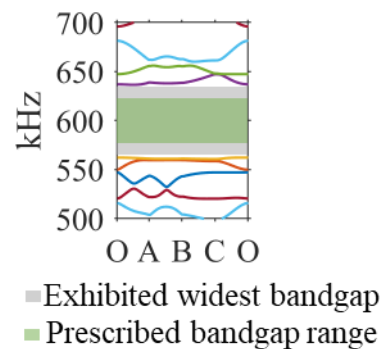


Figure 23 Design Point#2 perturbed unit cell and its corresponding band structure to demonstrate the accurate overlapping between its exhibited widest band gap and the prescribed band gap frequency range.

## Chapter 6. Conclusion

This work examined the potential of a new systematic design process for designing metamaterials with prescribed functional band gaps below the 1000kHz limit. This design process uses periodic perturbations to modify the morphology of simple lattices and enhance their band gap characteristics. Periodic perturbations with various amplitudes and frequencies were applied to a double-sided hexagonal honeycomb lattice with a relative having a range of relative densities (5%,10%,15%,20%,25% and 30%). The double-sided hexagonal lattice has a single narrow frequency band gap below the 1000kHz frequency. Modifying its morphology by imposing periodic perturbation changed its behavior and allowed it to exhibit many band gaps (around 30), with some reaching a width of~ 200kHz wide. The ability to increase the number of band gaps and their width indicates that periodic perturbations can be used to design metamaterials with prescribed band gaps systematically. A parametric study was conducted by varying the perturbation parameters, namely amplitude and frequency, as well as relative density. Results from the parametric study support the conclusions:

- 1) The perturbation parameters that result in the maximum number of band gaps can be different from those resulting in the frequency band gap with the maximum width.
- 2) The perturbation parameters that result in the widest frequency band gaps depend on relative density. In general, increasing the relative density lowered the perturbation parameters associated with the widest frequency band gaps. Accordingly, perturbations are more efficient in creating band gaps at lower relative densities.
- 3) Frequency band gaps dependence on perturbation parameters and relative density is complex and non-monotonic.

The complex relationship among frequency band gaps, relative density and perturbation parameters was modeled using multiple artificial neural networks (MANNs). Three parallel MANNs were developed to predict the key band gap features (i.e., width and centroid of the widest band gap as well as the number of band gaps) at each combination of perturbation parameters and relative density. Analysis of the MANNs' ability to predict the key band gap features supports the following conclusion:

- 1) The accuracy of the MANNs in predicting the width of the widest band gap ranged between 78.35%~99.94%, while their accuracy in predicting the centroid of the widest band gap ranged between 51.97%~100%. These accuracy levels allow the predicted band gap to overlap with the actual band gap substantially.
- 2) The accuracy of the MANNs in predicting the number of band gaps ranged between 79.68%-99.94%.

The level of accuracy provided by the MANNs allows for predicting the perturbation parameters needed to realize a predetermined band gap. Accordingly, this work shows that metamaterials exhibiting a desired band gap below the 1000kHz frequency can be designed using sinusoidal perturbations, the simple hexagonal lattice, and the developed MANNs.

## References

- [1] P. Zhao, K. Zhang, and Z. Deng, “Elastic Wave Propagation in Lattice Metamaterials with Koch Fractal,” *Acta Mechanica Solida Sinica*, vol. 33, no. 5, pp. 600–611, Oct. 2020, doi: 10.1007/s10338-020-00177-w.
- [2] P. Zhao, K. Zhang, C. Zhao, and Z. Deng, “Mechanism of Band Gaps in Self-Similar Triangular Lattice With Koch Fractal,” *J Vib Acoust*, vol. 144, no. 3, Jun. 2022, doi: 10.1115/1.4052944.
- [3] M. J. Choi, M. H. Oh, B. Koo, and S. Cho, “Optimal design of lattice structures for controllable extremal band gaps,” *Sci Rep*, vol. 9, no. 1, Dec. 2019, doi: 10.1038/s41598-019-46089-9.
- [4] Y. Chen, F. Qian, L. Zuo, F. Scarpa, and L. Wang, “Broadband and Multiband Vibration Mitigation in Lattice Metamaterials with Sinusoidally-shaped Ligaments,” *Extreme Mech Lett*, vol. 17, pp. 24–32, Nov. 2017, doi: 10.1016/j.eml.2017.09.012.
- [5] M. Alkhader and M. Vural, “A plasticity model for pressure-dependent anisotropic cellular solids,” *Int J Plast*, vol. 26, no. 11, pp. 1591–1605, 2010.
- [6] M. Alkhader and M. Vural, “The partition of elastic strain energy in solid foams and lattice structures,” *Acta Mater*, vol. 57, no. 8, pp. 2429–2439, 2009, doi: 10.1016/j.actamat.2009.01.034.
- [7] M. Alkhader and M. Vural, “Mechanical response of cellular solids: Role of cellular topology and microstructural irregularity,” *Int J Eng Sci*, vol. 46, no. 10, pp. 1035–1051, 2008, doi: 10.1016/j.ijengsci.2008.03.012.
- [8] M. Alkhader and M. Vural, “An energy-based anisotropic yield criterion for cellular solids and validation by biaxial FE simulations,” *J Mech Phys Solids*, vol. 57, no. 5, pp. 871–890, 2009, doi: 10.1016/j.jmps.2008.12.005.
- [9] A. K. Kaw, *Mechanics of composite materials*. Taylor & Francis, 2006.
- [10] I. M. Daniel and Ori. Ishai, *Engineering mechanics of composite materials*. Oxford University Press, 2006.

- [11] M. Alkhader, S. Iyer, W. Shi, and T. Venkatesh, “Low frequency acoustic characteristics of periodic honeycomb cellular cores: The effect of relative density and strain fields,” *Compos Struct*, vol. 133, pp. 77–84, Jan. 2015, doi: 10.1016/j.compstruct.2015.07.102.
- [12] M. Ruzzene and F. Scarpa, “Directional and band-gap behavior of periodic auxetic lattices,” *physica status solidi (b)*, vol. 242, pp. 665–680, Jan. 2005, doi: 10.1002/pssb.200460385.
- [13] A. Spadoni, M. Ruzzene, S. Gonella, and F. Scarpa, “Phononic properties of hexagonal chiral lattices,” *Wave Motion*, vol. 46, pp. 435–450, Jan. 2009, doi: 10.1016/j.wavemoti.2009.04.002.
- [14] M. Alkhader, B. Abu-Nabah, M. Elyoussef, and T. A. Venkatesh, “Design of honeycomb structures with tunable acoustic properties,” *MRS Adv*, vol. 4, no. 44–45, pp. 2409–2418, Sep. 2019, doi: 10.1557/adv.2019.355.
- [15] S. Iyer, M. Alkhader, and T. A. Venkatesh, “Electromechanical behavior of auxetic piezoelectric cellular solids,” *Scr Mater*, vol. 99, pp. 65–68, Apr. 2015, doi: 10.1016/j.scriptamat.2014.11.030.
- [16] A. Ahmad, M. Alkhader, B. A. Abu-Nabah, and T. A. Venkatesh, “Effect of deformation mechanisms on in-plane wave propagation in periodic cellular materials,” *Waves in Random and Complex Media*, vol. 0, no. 0, pp. 1–23, 2021, doi: 10.1080/17455030.2021.1902017.
- [17] A. S. Phani, J. Woodhouse, N. Fleck, and N. A. Fleck, “Wave propagation in two-dimensional periodic lattices,” *Journal of the Acoustical Society of America*, vol. 119, no. 4, pp. 1995–2005, 2006, doi: 10.1121/1.2179748.
- [18] S. Iyer, M. Alkhader, and T. A. ; Venkatesh, “Band Gaps in Bravais Lattices Inspired Periodic Cellular Materials and The Effect of Relative Density and Strain Fields ,” in *ASME 2014 International Mechanical Engineering Congress & Exposition*, 2014.
- [19] S. Iyer, M. Alkhader, and T. A. Venkatesh, “On the relationships between cellular structure, deformation modes and electromechanical properties of

- piezoelectric cellular solids,” *Int J Solids Struct*, vol. 80, pp. 73–83, 2016, doi: <https://doi.org/10.1016/j.ijsolstr.2015.10.024>.
- [20] S. Iyer, M. Alkhader, and T. A. Venkatesh, “Electromechanical Response of Piezoelectric Honeycomb Foam Structures,” *Journal of the American Ceramic Society*, vol. 97, no. 3, pp. 826–834, 2014, doi: 10.1111/jace.12699.
- [21] A. Bayat and S. Gaitanaros, “Wave Directionality in Three-Dimensional Periodic Lattices,” *Journal of Applied Mechanics, Transactions ASME*, vol. 85, no. 1, Jan. 2018, doi: 10.1115/1.4038287.
- [22] H. el Mir, M. Alkhader, P. D. Pour, and M. Mustafa, “Improving the buckling strength of honeycomb cores using periodic imperfections,” in *2020 Advances in Science and Engineering Technology International Conferences (ASET)*, 2020, pp. 1–6. doi: 10.1109/ASET48392.2020.9118353.
- [23] J. Hou, Z. Zhang, and D. Li, “Numerical and experimental study on bandgap property of two-dimensional lattice with nested core,” *Appl Phys A Mater Sci Process*, vol. 128, no. 2, Feb. 2022, doi: 10.1007/s00339-022-05280-y.
- [24] C. Gao, V. Slesarenko, M. C. Boyce, S. Rudykh, and Y. Li, “Instability-Induced Pattern Transformation in Soft Metamaterial with Hexagonal Networks for Tunable Wave Propagation,” *Sci Rep*, vol. 8, no. 1, Dec. 2018, doi: 10.1038/s41598-018-30381-1.
- [25] S. Macrae Montgomery *et al.*, “Magneto-Mechanical Metamaterials with Widely Tunable Mechanical Properties and Acoustic Bandgaps.”
- [26] G. Y. Zhang and X. L. Gao, “Elastic wave propagation in 3-D periodic composites: Band gaps incorporating microstructure effects,” *Compos Struct*, vol. 204, pp. 920–932, Nov. 2018, doi: 10.1016/j.compstruct.2018.07.115.
- [27] F. Casadei, J. J. Rimoli, and M. Ruzzene, “Multiscale finite element analysis of wave propagation in periodic solids,” *Finite Elements in Analysis and Design*, vol. 108, pp. 81–95, Jan. 2016, doi: 10.1016/j.finel.2015.10.002.
- [28] J.-H. Bastek, S. Kumar, B. Telgen, R. N. Glaesener, and D. M. Kochmann, “Inverting the structure-property map of truss metamaterials by deep learning,”

*Proceedings of the National Academy of Sciences*, vol. 119, no. 1, 2021, doi: 10.1073/pnas.2111505119/-/DCSupplemental.

- [29] S. Lee, Z. Zhang, and G. X. Gu, “Generative machine learning algorithm for lattice structures with superior mechanical properties,” *Mater Horiz*, vol. 9, no. 3, pp. 952–960, Mar. 2022, doi: 10.1039/d1mh01792f.
- [30] W. Muhammad, A. P. Brahme, O. Ibragimova, J. Kang, and K. Inal, “A Machine Learning Framework to Predict Local Strain Distribution and the Evolution of Plastic Anisotropy & Fracture in Additively Manufactured Alloys,” *Int J Plast*, vol. 136, Jan. 2021, doi: 10.1016/j.ijplas.2020.102867.
- [31] M. Alkhader, W. Abuzaid, M. Elyoussef, and S. Al-Adaileh, “Localized strain fields in honeycomb materials with convex and concaved cells,” *European Journal of Mechanics - A/Solids*, p. 103890, 2019, doi: <https://doi.org/10.1016/j.euromechsol.2019.103890>.
- [32] L. J. Gibson and M. F. Ashby, “The mechanics of honeycombs,” in *Cellular Solids: Structure and Properties*, 2nd ed., Cambridge: Cambridge University Press, 1997, pp. 93–174.
- [33] S. Balawi and J. L. Abot, “The effect of honeycomb relative density on its effective in-plane elastic moduli: An experimental study,” *Compos Struct*, vol. 84, no. 4, pp. 293–299, 2008, doi: <https://doi.org/10.1016/j.compstruct.2007.08.009>.
- [34] A. Ahmed, M. Alkhader, and B. Abu-Nabah, “In-plane elastic wave propagation in aluminum honeycomb cores fabricated by bonding corrugated sheets,” *Journal of Sandwich Structures & Materials*, vol. 21, no. 8, pp. 2949–2974, 2019.
- [35] M. Ruzzene and F. Scarpa, “Directional and band-gap behavior of periodic auxetic lattices,” *physica status solidi (b)*, vol. 242, no. 3, pp. 665–680, 2005, doi: 10.1002/pssb.200460385.
- [36] K. Bertoldi and M. C. Boyce, “Mechanically triggered transformations of phononic band gaps in periodic elastomeric structures,” *Phys Rev B*, vol. 77, no. 5, p. 52105, 2008, doi: 10.1103/PhysRevB.77.052105.

- [37] L. Brillouin, *Wave propagation in periodic structures: electric filters and crystal lattices*. DoverPublications. com, 2003, pp.102-105.
- [38] M. A. Jaradat, M. F. Abdel-Hafez, K. Saadeddin, and M. A. Jarrah, “Intelligent fault detection and fusion for INS/GPS navigation system,” in *2013 9th International Symposium on Mechatronics and Its Applications, ISMA 2013*, 2013. doi: 10.1109/ISMA.2013.6547398.
- [39] W. Abuzaid, M. Alkhader, and M. Omari, “Experimental analysis of heterogeneous shape recovery in 4d printed honeycomb structures,” *Polym Test*, vol. 68, pp. 100–109, 2018, doi: <https://doi.org/10.1016/j.polymertesting.2018.03.050>.
- [40] M. H. Yousuf, W. Abuzaid, and M. Alkhader, “4D printed auxetic structures with tunable mechanical properties,” *Addit Manuf*, vol. 35, p. 101364, Jun. 2020, doi: ARTN 101364 10.1016/j.addma.2020.101364.

## Vita

Mohamed Shendy was born in 1998, in Sharjah, United Arab Emirates. He received his primary and secondary education in Dubai, UAE. He received his B.Sc. degree in Aeronautical Engineering from Emirates Aviation University in 2020.

In January 2021, he joined the Mechanical Engineering master's program in the American University of Sharjah as a graduate teaching assistant. His research interests are in Programmable Metamaterials, Acoustics, Mechanical Vibrations, Computational Mechanics, Finite Elements and Artificial Intelligent Systems.